
NON-PARAMETRIC MONITORING OF SPATIAL DEPENDENCE

A PREPRINT

Philipp Adämmer 

Institute of Data Science

University of Greifswald

Greifswald, Germany

philipp.adaemmer@uni-greifswald.de

Philipp Wittenberg 

Department of Mathematics and Statistics

Helmut Schmidt University

Hamburg, Germany

pwitten@hsu-hh.de

Christian H. Weiß *

Department of Mathematics and Statistics

Helmut Schmidt University

Hamburg, Germany

weissc@hsu-hh.de

Murat Caner Testik 

Hacettepe University

Department of Industrial Engineering

Beytepe-Ankara, Türkiye

mtestik@hacettepe.edu.tr

ABSTRACT

In process monitoring applications, measurements are often taken regularly or randomly from different spatial locations in two or three dimensions. Here, we consider streams of regular, rectangular data sets and use spatial ordinal patterns (SOPs) as a non-parametric approach to detect spatial dependencies. A key feature of our proposed SOP charts is that they are distribution-free and do not require prior Phase-I analysis. We conduct an extensive simulation study, demonstrating the superiority and effectiveness of the proposed charts compared to traditional parametric approaches. We apply the SOP-based control charts to detect heavy rainfall in Germany, war-related fires in (eastern) Ukraine, and manufacturing defects in textile production. The wide range of applications and insights illustrate the broad utility of our non-parametric approach.

Keywords: non-parametric control charts; ordinal patterns; regular lattice data; spatial dependence; spatial processes.

* corresponding author

1 Introduction

In 2024, we celebrate the centenary of the control chart, which was first proposed by Walter A. Shewhart as part of his famous memorandum from May 16, 1924, at the Bell Telephone Laboratories (see [Olmstead, 1967](#)). Over the years, control charts have proven to be very effective tools for monitoring processes and many control charts have been developed depending on the different characteristics of measurements.

During the last two decades, the use of ordinal patterns (OPs), which were originally introduced by [Bandt and Pompe \(2002\)](#), has become increasingly popular in time series analysis (see [Bandt \(2019, 2023\)](#) for recent surveys). Among others, OPs were utilized to construct non-parametric tests for serial dependence in univariate time series data (see [Weiß, 2022](#); [Weiß and Schnurr, 2024](#)). Related to this, recently [Weiß and Testik \(2023\)](#) utilized OPs in statistical process monitoring (SPM), where non-parametric control charts based on OPs were used to detect the occurrence of serial dependencies.

In the present study, we consider OP-based control charts for SPM of data that are collected as a regular two-dimensional grid (regular lattice data):

$$\begin{array}{cccc}
 y_{0,0}, & y_{0,1}, & \cdots & y_{0,n}, \\
 \vdots & \vdots & \ddots & \vdots \\
 y_{m,0}, & y_{m,1}, & \cdots & y_{m,n}.
 \end{array} \tag{1}$$

Here, we use the short-hand notation (y_s) for such a rectangular data set, where the spatial position $s = (s_1, s_2)$ takes values in $\{0, \dots, m\} \times \{0, \dots, n\}$ with $m, n \in \mathbb{N} = \{1, 2, \dots\}$. For the last few years, increasing attention has been paid to monitoring streams of such rectangular data in the SPM literature (see e. g., [Megahed et al. \(2011\)](#); [Colosimo \(2018\)](#) for surveys). Especially, applications related to (video-)image data have been reported, covering quality-related areas (e. g., monitoring of phone displays or textile images) as well as health surveillance (see [Wang and Tsung \(2005\)](#); [Jiang et al. \(2011\)](#); [Megahed et al. \(2012\)](#); [Bui and Apley \(2018\)](#); [Tsiamirtzis et al. \(2022\)](#) for details and further references). Some earlier research also considered vector representation of streams of spatial positions. For instance, [Runger and Fowler \(1998\)](#) considered the wafer fabrication step of an integrated circuits manufacturing process, where silicon dioxide thickness measurements were taken from nine sites on each of four wafers in a furnace at each run. As there is additional information from many wafers and sites in a run, to be sensitive to particular process upsets, such as differences between locations of wafers in the furnace and/or between sites on a wafer, linear combinations of measurements are analyzed by the analysis of variance method to develop control charts. Another manufacturing example for monitoring rectangular data, the multilayer chip capacitors process described by [Barton and Gonzalez-Barreto \(1996\)](#), is briefly discussed later in Remark 4.1.1. A survey of automated visual-based defect detection approaches in industrial applications for detecting defects on surfaces through images can be found in [Czimmermann et al. \(2020\)](#). However, monitoring streams of rectangular data sets is not limited to traditional SPM applications. In Section 5, in addition to a manufacturing example, we also consider geographic data on weather events and war-related fires.

In what follows, we monitor streams of rectangular data for possible spatial dependence. To do this, we develop non-parametric control charts based on spatial OPs (SOPs). Such SOPs, which constitute an extension of OPs to the plane, were first proposed by [Ribeiro et al. \(2012\)](#) and studied in detail by [Bandt and Wittfeld \(2023\)](#). A comprehensive discussion is provided in Section 2. The corresponding control charts are proposed in Section 3, where we also consider control charts based on the spatial autocorrelation function (ACF) as a competing (but parametric) monitoring approach. Section 4 and Appendix A present the results of a comprehensive simulation study that examines the

average run length (ARL) performance of the proposed SOP charts with respect to various out-of-control scenarios. The relevance of the SOP charts and their application in practice is demonstrated in Section 5, where three real-world examples (precipitation data, war-related fires, and textile images) are discussed. Finally, Section 6 concludes and outlines directions for future research.

2 Spatial Ordinal Patterns and Types

Let (y_s) be a rectangular data set as given in (1), which is assumed to originate from some stationary spatial process in the plane (random field), say $(Y_s) = (Y_s)_{s \in \mathbb{Z}^2}$ with $\mathbb{Z} = \{\dots, -1, 0, 1, \dots\}$, where the Y_s are real-valued and continuously distributed random variables (RVs). According to [Ribeiro et al. \(2012\)](#), a SOP is computed by first picking out a $w_1 \times w_2$ -rectangle from the data (y_s) , where $w_1, w_2 \geq 2$. Then, the original real numbers are replaced by integer ranks from $\{1, 2, \dots, w_1 \cdot w_2\}$, leading to one of the $(w_1 \cdot w_2)!$ different SOPs of order $w_1 \cdot w_2$. As rank statistics, SOPs are robust against outliers, and their distribution does not depend on the actual (continuous) marginal distribution of (Y_s) . The importance of SOPs for developing non-parametric (distribution-free) approaches for dependence analysis arises from the fact that under the additional assumption of spatial independence, i. e., if (Y_s) is independent and identically distributed (i. i. d.), the SOPs follow a discrete uniform distribution with probability $1/(w_1 \cdot w_2)!$ for each SOP, see [Bandt and Wittfeld \(2023\)](#); [Weiß and Kim \(2024\)](#) for details. Therefore, if testing the null hypothesis of the spatial independence of (Y_s) against spatial dependence, one uses test statistics that compare the SOPs' actual distribution to the discrete uniform one. However, the uniform probability $1/(w_1 \cdot w_2)!$ gets rather small for $w_1 \cdot w_2 > 4$ such that the different SOPs are hardly observed with reasonable frequency in practice. For this reason, like in [Bandt and Wittfeld \(2023\)](#); [Weiß and Kim \(2024\)](#), we restrict our discussion to 2×2 -SOPs (i. e., $w_1 = w_2 = 2$), where always one of the 24 possible squares of ranks from $\mathcal{S} = \left\{ \boldsymbol{\pi} = \begin{pmatrix} r_1 & r_2 \\ r_3 & r_4 \end{pmatrix} \mid \{r_1, r_2, r_3, r_4\} = \{1, 2, 3, 4\} \right\}$ is observed. Denoting the extracted 2×2 -rectangle by $\mathbf{Y} =: \begin{pmatrix} y_1 & y_2 \\ y_3 & y_4 \end{pmatrix}$, i. e., the entries are read row-by-row, the corresponding SOP $\boldsymbol{\pi} = \begin{pmatrix} r_1 & r_2 \\ r_3 & r_4 \end{pmatrix}$ is defined by

$$r_k < r_l \quad \Leftrightarrow \quad y_k < y_l \quad \text{or} \quad (y_k = y_l \text{ and } k < l) \quad (2)$$

for all $\{k, l\} \subset \{1, 2, 3, 4\}$. Note that this definition covers the case of ties within \mathbf{Y} , although ties are observed with probability 0 for continuously distributed RVs. In practice, however, due to the limited numerical precision of measurement devices, ties in \mathbf{Y} might occasionally be observed.

If analyzing (y_s) for spatial dependence, we do not only extract a single 2×2 -square for SOP computation, but all $m \cdot n$ possible squares $\mathbf{Y}_s = \begin{pmatrix} y_{s_1-1, s_2-1} & y_{s_1-1, s_2} \\ y_{s_1, s_2-1} & y_{s_1, s_2} \end{pmatrix}$ for $s \in \{1, \dots, m\} \times \{1, \dots, n\}$. It would also be possible to consider further integer “delay parameters” $d_1, d_2 \geq 1$ (spatial lags) and to extract squares of the form $\begin{pmatrix} y_{s_1-d_1, s_2-d_2} & y_{s_1-d_1, s_2} \\ y_{s_1, s_2-d_2} & y_{s_1, s_2} \end{pmatrix}$. However, we focus on $d_1 = d_2 = 1$ as first-order dependence is often most pronounced in applications. Then, one determines the vector of relative frequencies of all SOPs to estimate the true SOP probabilities, where deviations from $(\frac{1}{24}, \dots, \frac{1}{24})^\top$ indicate the presence of spatial dependence. Note that for (Y_s) being i. i. d., [Weiß and Kim \(2024\)](#) proved asymptotic normality for the SOP frequencies and derived a closed-form expression for their covariance matrix.

Although we already focus on the smallest possible SOPs, their frequencies will commonly be rather low unless the sample size $m \cdot n$ is very large. For this reason, [Bandt and Wittfeld \(2023\)](#) proposed a partition of \mathcal{S} into larger subsets and to determine the frequencies with respect to these subsets only. More precisely, each SOP $\boldsymbol{\pi} \in \mathcal{S}$ is assigned to one out of three possible “types”, where $\boldsymbol{\pi}$ is said to have type $k \in \{1, 2, 3\}$ iff $\boldsymbol{\pi} \in \mathcal{S}_k$, with the subsets \mathcal{S}_k of size 8

being defined as

$$\begin{aligned}
 \mathcal{S}_1 &= \left\{ \begin{pmatrix} \mathbf{1} & \mathbf{2} \\ \mathbf{3} & \mathbf{4} \end{pmatrix}, \begin{pmatrix} \mathbf{1} & \mathbf{3} \\ \mathbf{2} & \mathbf{4} \end{pmatrix}, \begin{pmatrix} \mathbf{2} & \mathbf{1} \\ \mathbf{4} & \mathbf{3} \end{pmatrix}, \begin{pmatrix} \mathbf{2} & \mathbf{4} \\ \mathbf{1} & \mathbf{3} \end{pmatrix}, \begin{pmatrix} \mathbf{3} & \mathbf{1} \\ \mathbf{4} & \mathbf{2} \end{pmatrix}, \begin{pmatrix} \mathbf{3} & \mathbf{4} \\ \mathbf{1} & \mathbf{2} \end{pmatrix}, \begin{pmatrix} \mathbf{4} & \mathbf{2} \\ \mathbf{3} & \mathbf{1} \end{pmatrix}, \begin{pmatrix} \mathbf{4} & \mathbf{3} \\ \mathbf{2} & \mathbf{1} \end{pmatrix} \right\}, \\
 &\quad \text{(monotonic behaviour along both rows and columns)} \\
 \mathcal{S}_2 &= \left\{ \begin{pmatrix} \mathbf{1} & \mathbf{2} \\ \mathbf{4} & \mathbf{3} \end{pmatrix}, \begin{pmatrix} \mathbf{1} & \mathbf{4} \\ \mathbf{2} & \mathbf{3} \end{pmatrix}, \begin{pmatrix} \mathbf{2} & \mathbf{1} \\ \mathbf{3} & \mathbf{4} \end{pmatrix}, \begin{pmatrix} \mathbf{2} & \mathbf{3} \\ \mathbf{1} & \mathbf{4} \end{pmatrix}, \begin{pmatrix} \mathbf{3} & \mathbf{2} \\ \mathbf{4} & \mathbf{1} \end{pmatrix}, \begin{pmatrix} \mathbf{3} & \mathbf{4} \\ \mathbf{2} & \mathbf{1} \end{pmatrix}, \begin{pmatrix} \mathbf{4} & \mathbf{1} \\ \mathbf{3} & \mathbf{2} \end{pmatrix}, \begin{pmatrix} \mathbf{4} & \mathbf{3} \\ \mathbf{1} & \mathbf{2} \end{pmatrix} \right\}, \\
 &\quad \text{(uniquely increase/decrease along either rows or columns)} \\
 \mathcal{S}_3 &= \left\{ \begin{pmatrix} \mathbf{1} & \mathbf{3} \\ \mathbf{4} & \mathbf{2} \end{pmatrix}, \begin{pmatrix} \mathbf{1} & \mathbf{4} \\ \mathbf{3} & \mathbf{2} \end{pmatrix}, \begin{pmatrix} \mathbf{2} & \mathbf{3} \\ \mathbf{4} & \mathbf{1} \end{pmatrix}, \begin{pmatrix} \mathbf{2} & \mathbf{4} \\ \mathbf{3} & \mathbf{1} \end{pmatrix}, \begin{pmatrix} \mathbf{3} & \mathbf{1} \\ \mathbf{2} & \mathbf{4} \end{pmatrix}, \begin{pmatrix} \mathbf{3} & \mathbf{2} \\ \mathbf{1} & \mathbf{4} \end{pmatrix}, \begin{pmatrix} \mathbf{4} & \mathbf{1} \\ \mathbf{2} & \mathbf{3} \end{pmatrix}, \begin{pmatrix} \mathbf{4} & \mathbf{2} \\ \mathbf{1} & \mathbf{3} \end{pmatrix} \right\}. \\
 &\quad \text{(both lowest and both highest ranks on a diagonal)}
 \end{aligned} \tag{3}$$

It is easily verified from (3), see the ranks printed in bold font, that the type of the SOP $\boldsymbol{\pi} = \begin{pmatrix} r_1 & r_2 \\ r_3 & r_4 \end{pmatrix}$ is recognized as that rank number which shares a diagonal with the rank 4. As indicated in parentheses in (3), the different types are well interpretable; see [Bandt and Wittfeld \(2023\)](#). Under the i. i. d. assumptions, the types are again uniformly distributed, namely with probability vector $\boldsymbol{p} = \left(\frac{1}{3}, \frac{1}{3}, \frac{1}{3}\right)^\top$. For their relative frequencies $\hat{\boldsymbol{p}}$, closed-form normal asymptotics have been derived by [Wei and Kim \(2024\)](#).

To analyze for spatial dependence, the following pairs of statistics based on $\hat{\boldsymbol{p}}$ have been proposed by [Bandt and Wittfeld \(2023\)](#):

$$\begin{aligned}
 \hat{\tau} &= \hat{p}_1 - 1/3 \quad \text{and} \quad \hat{\kappa} = \hat{p}_2 - \hat{p}_3, \\
 \tilde{\tau} &= \hat{p}_3 - 1/3 \quad \text{and} \quad \tilde{\kappa} = \hat{p}_1 - \hat{p}_2.
 \end{aligned} \tag{4}$$

Again, asymptotic normality holds, and deviations from zero are indicators of spatial dependence. While [Bandt and Wittfeld \(2023\)](#) recommend $\hat{\tau}$ and $\hat{\kappa}$ for applications in image analysis, [Wei and Kim \(2024\)](#) found the $\tilde{\tau}$ -test to show the best power with respect to various spatial data generating processes (DGPs). For their simulation study, they also considered the spatial ACF $\rho(\boldsymbol{h}) = \text{Corr}[Y_{\boldsymbol{s}}, Y_{\boldsymbol{s}-\boldsymbol{h}}]$ as a competitor, where they focused on the spatial lag $\boldsymbol{h} = \mathbf{1} = (1, 1)^\top$ in accordance to the choice $d_1 = d_2 = 1$ for the delay parameters. More precisely, they applied the corresponding sample version $\hat{\rho}(\mathbf{1}) = (\sum_{\boldsymbol{s}} (Y_{\boldsymbol{s}} - \bar{Y})(Y_{\boldsymbol{s}-\mathbf{1}} - \bar{Y})) / (\sum_{\boldsymbol{s}} (Y_{\boldsymbol{s}} - \bar{Y})^2)$ with \bar{Y} denoting the sample mean, see [Meyer et al. \(2017\)](#) for the asymptotics. While the $\hat{\rho}(\mathbf{1})$ -test is well-suited for uncovering linear dependence in $(Y_{\boldsymbol{s}})$, as it is caused by unilateral spatial autoregressive (SAR) processes, SOP-based tests from (4) turned out be advantageous for non-linear or bilateral DGPs, and for unilateral linear processes in the presence of outliers or zero inflation (see [Wei and Kim, 2024](#)).

2.1 Example To illustrate the computation of SOPs and their types, let us analyze one of the data examples discussed by [Grimshaw et al. \(2013, p. 135\)](#), shown in Figure 1 (a). For evaluating the quality of a manufactured bottle, its thickness (in inches) is measured at regular spatial locations \boldsymbol{s} around the cylindrical surface (5×5 grid, so $m = n = 4$), and the rectangular data set in (a) results from unwrapping the surface. A plot of the data, where increasing darkness expresses increasing thickness, is shown in Figure 1 (b). The SOPs corresponding to the 2×2 -squares at locations $\boldsymbol{s} \in \{1, \dots, 4\}^2$ (bottom-right corner of extracted squares) are shown in (c), and the resulting types in (d). The highlighted 2×2 -square at $\boldsymbol{s} = (3, 2)$ is one out of three cases where a tie is observed (twice the value “0.0596”), which is caused by the limited measurement precision (units of 0.0001 inch). Definition (2) accounts for the tie by assigning the lower rank to the first occurrence of “0.0596”.

The type frequencies implied by Figure 1 (d), $\hat{\boldsymbol{p}} = (0.5625, 0.4375, 0.0000)^\top$, deviate considerably from the probability vector $\boldsymbol{p} = \left(\frac{1}{3}, \frac{1}{3}, \frac{1}{3}\right)^\top$ expected under spatial independence. In particular, type 3 is never observed. The statistics in (4) take the values $\hat{\tau} \approx 0.229 (\pm 0.239)$, $\hat{\kappa} \approx 0.438 (\pm 0.424)$, $\tilde{\tau} \approx -0.333 (\pm 0.248)$, and $\tilde{\kappa} \approx 0.125 (\pm 0.410)$, respectively, where the critical values (5%-level) shown in parentheses are computed according to [Wei and Kim \(2024\)](#). So $\hat{\kappa}$ and $\tilde{\tau}$ indicate significant spatial dependence, which seems plausible as these two statistics depend on \hat{p}_3 . By contrast, $\hat{\rho}(\mathbf{1}) \approx 0.301$ does not violate its critical values ± 0.392 , with the latter being computed according to [Meyer et al. \(2017\)](#). Certainly, any of these test decisions should be

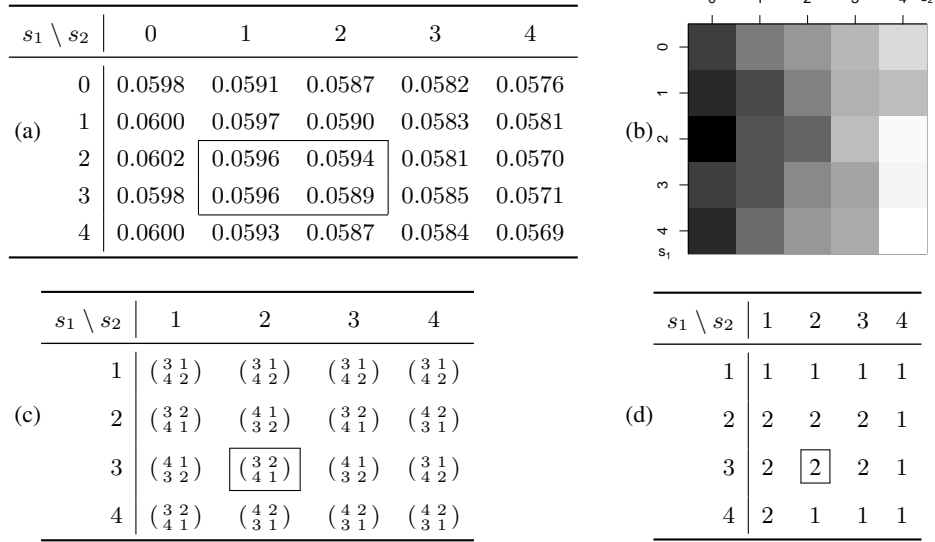


Figure 1: Bottle thickness data from Example 2.1 in (a), the corresponding plot in (b), computed SOPs in (c), and types in (d). Highlighted 2×2 -square in (a) leads to highlighted SOP and type in (c) and (d), respectively.

interpreted cautiously because the sample size is very small, so the validity of asymptotic approximations is questionable. However, spatial dependence is also supported by Figure 1 (b), where a kind of decreasing trend from left to right is visible. Note that such visual representations are especially useful as they provide fault diagnostic information in practice.

Let us conclude this section with a discussion of the problem of ties. Up to now, we assumed that the rectangular data sets (y_s) originate from continuously distributed RVs (Y_s) such that ties have probability zero. Nevertheless, ties might be observed in practice due to limited measurement precision, as demonstrated by Example 2.1, yet usually with negligible frequency. However, things change if the rectangular data originate from discrete RVs, such as count RVs with the range being contained in the set of non-negative integers, $\mathbb{N}_0 = \{0, 1, \dots\}$. To distinguish the discrete integer case from the continuous real-valued one, let us use the letters X, x instead of Y, y for denoting the RVs and data, respectively (although we restrict to X, x being integer-valued, the case of ordinal RVs and data is covered as well because the order information required for SOP-computation is already contained in the integer rank counts corresponding to the ordinal categories, see Weiß and Schnurr (2024) for details). For such discrete RVs (X_s) , ties occur with positive probability, and the frequency of ties in given data (x_s) might be quite large (also see Weiß and Schnurr (2024); Weiß and Kim (2024) for related discussions). Then, it is not recommended anymore to handle the ties according to definition (2) since this might cause a notable bias in estimating the true distribution of SOPs and types.

However, it is still possible to adapt the aforementioned SOP methodology to the integer case, namely by using a randomization approach (“jittering”, see Machado and Silva, 2005) as proposed by Weiß and Kim (2024). More precisely, before computing the SOPs and types, we first add i. i. d. uniform noise $(U_s) \sim U(0, 1)$ to the discrete integer RVs (X_s) , where $U(0, 1)$ denotes the uniform distribution in the open interval $(0; 1)$. Then, the resulting

$$Y_s := X_s + U_s \quad \text{with the noise } (U_t) \text{ being i. i. d. } U(0, 1) \quad (5)$$

are continuously distributed RVs such that ties occur with probability zero. Moreover, if (X_s) are even i. i. d., then the SOPs and types computed from (Y_s) are again discrete uniformly distributed such that the tests based on (4) are

still of non-parametric nature. Furthermore, the added noise only affects the ranks within the ties, whereas $X_r < X_s$ necessarily implies that also $Y_r < Y_s$, i. e., strict orders in (X_s) are always preserved. An unavoidable drawback of this randomization approach, however, is given by the fact that the actual outcome of the SOP analysis, e. g., computed value of the statistics $\tilde{\tau}$, depends on the chosen noise. This issue is discussed in more detail later in Section 5.

3 Non-parametric Control Charts for Spatial Dependence

In what follows, we are concerned with monitoring a *stream* of rectangular data sets, as it arises, for example, in the SPM applications surveyed in Section 1. Formally, the DGP is given by $[(Y_s^{(t)})_s]_t$, where $t \in \mathbb{N}$ and $s \in \{0, \dots, m\} \times \{0, \dots, n\}$. In the case of integer-valued RVs $X_s^{(t)}$, we first transform them into real-valued RVs $Y_s^{(t)}$ by adding uniform noise according to (5). We assume that the rectangular sets $(Y_s^{(t)})_s$ are generated independently of each other for different t . However, the RVs within the t th rectangular set $(Y_s^{(t)})_s$ can follow any joint distribution, which is specified by the in-control (IC) assumption and might differ for different applications. For the simulation study described in Section 4, the following IC-assumption is considered:

(IC-iid) For each $t \in \mathbb{N}$, $(Y_s^{(t)})_s$ is i. i. d. with continuous distribution.

The out-of-control (OOC) situations to be detected, in turn, are rectangular set $(Y_s^{(t)})_s$ exhibiting spatial dependence.

For process monitoring, it is suggested to use the t th data set $(Y_s^{(t)})_s$ for the computation of SOPs and types, and to derive the corresponding vector \hat{p}_t of type frequencies. Hence, altogether, the process $[(Y_s^{(t)})_s]_t$ is transformed into the process $(\hat{p}_t)_t$ of frequency vectors, which are then used for constructing control charts. Note that under the assumption of “IC-iid”, as explained in Section 2, the SOPs and types computed from $(Y_s^{(t)})_s$ are discrete uniformly distributed, independent of the actual distribution of the $Y_s^{(t)}$. In particular, the process $(\hat{p}_t)_t$ is i. i. d. with $E[\hat{p}_t] = (\frac{1}{3}, \frac{1}{3}, \frac{1}{3})^\top$. This shall allow us to define non-parametric control charts in this case.

In analogy to [Weiß and Testik \(2023\)](#), we distinguish two general approaches for monitoring $(\hat{p}_t)_t$:

- If the t th control statistic is computed solely based on \hat{p}_t , then we obtain a so-called Shewhart control chart (see [Montgomery, 2009](#)), which is classified as being memory-less because the previous \hat{p}_u , $u < t$, do not affect the t th control statistic.
- To attain a control chart with an inherent memory, we use an exponentially weighted moving average (EWMA) approach (see [Roberts, 1959](#)), where a smoothing parameter $\lambda \in (0; 1)$ as well as an initial probability vector p_0 for the types have to be specified, and where

$$\hat{p}_0^{(\lambda)} = p_0, \quad \hat{p}_t^{(\lambda)} = \lambda \hat{p}_t + (1 - \lambda) \hat{p}_{t-1}^{(\lambda)} \quad \text{for } t = 1, 2, \dots \quad (6)$$

is computed. Then, $\hat{p}_t^{(\lambda)}$ is used for calculating the t th control statistic.

It is well known that the EWMA’s λ controls the strength of the inherent memory, with increasing memory for decreasing λ , see [Roberts \(1959\)](#). Note that the boundary case $\lambda \rightarrow 1$ leads to the aforementioned Shewhart approach, so it is sufficient to introduce the subsequent control charts with respect to the sequence $(\hat{p}_t^{(\lambda)})$ computed via (6). The choice of p_0 (only relevant if $\lambda < 1$) depends on the actual IC-assumption; under the assumption of “IC-iid”, we choose $p_0 = (\frac{1}{3}, \frac{1}{3}, \frac{1}{3})^\top$.

Finally, we propose four classes of control charts, which are obtained by plugging in $\hat{\boldsymbol{p}}_t^{(\lambda)}$ into one of the four statistics defined in (4), and to plot the resulting sequence of statistics against symmetric two-sided control limits (CLs):

$$\begin{aligned}
 \widehat{\tau}\text{-chart: } & \text{plot } \widehat{\tau}_t^{(\lambda)} = \widehat{p}_{t,1}^{(\lambda)} - \frac{1}{3}, \quad \text{trigger alarm if } |\widehat{\tau}_t^{(\lambda)}| > l_{\widehat{\tau},\lambda}; \\
 \widehat{\kappa}\text{-chart: } & \text{plot } \widehat{\kappa}_t^{(\lambda)} = \widehat{p}_{t,2}^{(\lambda)} - \widehat{p}_{t,3}^{(\lambda)}, \quad \text{trigger alarm if } |\widehat{\kappa}_t^{(\lambda)}| > l_{\widehat{\kappa},\lambda}; \\
 \widetilde{\tau}\text{-chart: } & \text{plot } \widetilde{\tau}_t^{(\lambda)} = \widehat{p}_{t,3}^{(\lambda)} - \frac{1}{3}, \quad \text{trigger alarm if } |\widetilde{\tau}_t^{(\lambda)}| > l_{\widetilde{\tau},\lambda}; \\
 \widetilde{\kappa}\text{-chart: } & \text{plot } \widetilde{\kappa}_t^{(\lambda)} = \widehat{p}_{t,1}^{(\lambda)} - \widehat{p}_{t,2}^{(\lambda)}, \quad \text{trigger alarm if } |\widetilde{\kappa}_t^{(\lambda)}| > l_{\widetilde{\kappa},\lambda}.
 \end{aligned} \tag{7}$$

Chart design and performance evaluation shall be done based on ARL considerations. Specifically, we focus on the so-called ‘‘zero-state ARL’’ (see Knoth, 2006), which expresses the mean number of statistics plotted on a chart, right from the beginning of process monitoring at $t = 1$ until the first alarm. Furthermore, if the process deviates from the specified IC-model (i. e., if the process has changed into an OOC-state), then the zero-state ARL also assumes that this change already happened at $t = 1$. There exist further ARL concepts in the literature where a delayed change point is assumed, see Knoth (2006). However, for a Shewhart chart (case $\lambda = 1$), they all lead to the same ARL value, and for conventional EWMA charts such as defined in (6), the differences between the different ARL values are usually negligible for practice (also see the study by Weiß and Testik (2023) on related OP-based EWMA charts). Thus, we focus on the zero-state ARL, and we use it in a two-fold manner:

- If computed under IC-conditions, the resulting IC-ARL is used for chart design, i. e., the CL $l_{\cdot,\lambda}$ is chosen such that the considered chart’s IC-ARL is close to a specified target value ARL_0 (we use the common choice $ARL_0 = 370$ for illustration).
- If computed under OOC-conditions, the resulting OOC-ARL expresses the performance of the considered chart in detecting the process change.

The ARL values can be approximated based on simulations. For a given DGP scenario and chart design, one simulates R times the DGP and determines the time until the first alarm (i. e., the run length). The sample mean across these R run lengths provides an estimate of the true ARL. Recall that for the special case of assumption ‘‘IC-iid’’, the distribution of the process $(\widehat{\boldsymbol{p}}_t)_t$ does not depend on the distribution of the $Y_s^{(t)}$. Hence, our charts are non-parametric/distribution-free. Therefore, for ARL simulation, one can use any continuous distribution for the $Y_s^{(t)}$, e. g., a standard normal distribution.

3.1 Remark A natural competitor of our SOP-based control charts given in (7) for spatial dependence is an analogous control chart based on the spatial ACF (recall the discussion after (4)). Here, the idea is to compute $\hat{\rho}(1)$ from each data set $(Y_s^{(t)})_s$, and to use the obtained sequence of ACF values, say $(\widehat{\rho}_t)$, for process monitoring. In analogy to (6), this can be combined with an EWMA approach, as

$$\widehat{\rho}_t^{(\lambda)} = \rho_0, \quad \widehat{\rho}_t^{(\lambda)} = \lambda \widehat{\rho}_t + (1 - \lambda) \widehat{\rho}_{t-1}^{(\lambda)} \quad \text{for } t = 1, 2, \dots, \tag{8}$$

and an alarm is triggered at time t if $|\widehat{\rho}_t^{(\lambda)}| > l_{\widehat{\rho},\lambda}$. Under the assumption ‘‘IC-iid’’, the initial value is chosen as $\rho_0 = 0$. A fundamental difference is given by the fact that the distribution of $\hat{\rho}(1)$ depends on the one of $(Y_s^{(t)})_s$. So the $\widehat{\rho}$ -chart is of a parametric nature, and chart design requires a full specification of the in-control model. On the other hand, $\hat{\rho}(1)$ can also be computed from integer data $(X_s^{(t)})_s$, i. e., the $\widehat{\rho}$ -chart can be directly applied to $(X_s^{(t)})_s$ without prior randomization.

4 Simulation Study

To analyze the ARL performance of the control charts proposed in Section 3, we did a comprehensive simulation study covering various IC- and OOC-scenarios. To ensure a high quality of approximation, we used $R = 10^6$ replications

per scenario to determine the control limits and $R = 10^5$ replications to approximate the IC and OOC-ARLs for performance analyses. The selected DGPs and sample sizes m, n are similar to those used by Weiß and Kim (2024) in their research on SOP-based hypothesis testing, as this allows us to compare the ARL performance of our “sequential tests” with the power performance of their classical hypothesis tests. Since ARL simulations are much more time-consuming than power simulations, and to also make the continuous and discrete cases more balanced, we restrict to count distributions with mean 5 (“medium counts”).

Table 1: IC-designs of EWMA SOP-charts in (7) and $\hat{\rho}$ -chart in (8) for different m, n combinations, smoothing parameters λ , and target $ARL_0 \approx 370$; simulated with 10^6 replications. EWMA SOP-charts use $N(0, 1)$ simulations, $\hat{\rho}$ -charts use either $N(0, 1)$ or $Poi(5)$ simulations.

| m, n | λ | $\hat{\tau}$ -chart | | $\hat{\kappa}$ -chart | | $\tilde{\tau}$ -chart | | $\tilde{\kappa}$ -chart | | $\hat{\rho}$ -N(0, 1) | | $\hat{\rho}$ -Poi(5) | |
|--------|-----------|---------------------------|-------|-----------------------------|-------|-----------------------------|-------|-------------------------------|-------|---------------------------|-------|---------------------------|-------|
| | | $l_{\hat{\tau}, \lambda}$ | ARL | $l_{\hat{\kappa}, \lambda}$ | ARL | $l_{\tilde{\tau}, \lambda}$ | ARL | $l_{\tilde{\kappa}, \lambda}$ | ARL | $l_{\hat{\rho}, \lambda}$ | ARL | $l_{\hat{\rho}, \lambda}$ | ARL |
| 1, 1 | 0.05 | 0.18549 | 369.5 | 0.32399 | 370.3 | 0.18555 | 370.8 | 0.32398 | 370.3 | 0.15106 | 370.4 | 0.15059 | 369.7 |
| | 0.10 | 0.2809 | 370.7 | 0.49178 | 369.2 | 0.28085 | 369.9 | 0.49177 | 369.6 | 0.19448 | 369.2 | 0.19378 | 370.2 |
| | 0.25 | 0.48164 | 370.4 | 0.78644 | 370.3 | 0.48162 | 369.8 | 0.7864 | 370.8 | 0.28253 | 370.1 | 0.28117 | 369.9 |
| 10, 10 | 0.05 | 0.01962 | 370.2 | 0.03491 | 370.2 | 0.02042 | 370.3 | 0.03351 | 369.8 | 0.03537 | 370.5 | 0.03533 | 370.6 |
| | 0.10 | 0.03049 | 369.6 | 0.05426 | 369.7 | 0.03174 | 369.8 | 0.05209 | 370.1 | 0.05313 | 369.8 | 0.05305 | 369.5 |
| | 0.25 | 0.05386 | 370.1 | 0.09587 | 370.0 | 0.05611 | 369.9 | 0.09200 | 370.0 | 0.09137 | 370.5 | 0.09119 | 369.8 |
| 15, 15 | 0.05 | 0.0131 | 369.2 | 0.02333 | 370.4 | 0.01365 | 369.4 | 0.02237 | 369.9 | 0.02425 | 370.6 | 0.02423 | 370.5 |
| | 0.10 | 0.02036 | 369.7 | 0.03626 | 369.5 | 0.02122 | 369.7 | 0.03476 | 370.0 | 0.03701 | 369.7 | 0.03698 | 369.5 |
| | 0.25 | 0.03597 | 369.9 | 0.06408 | 369.7 | 0.03751 | 370.6 | 0.06142 | 369.9 | 0.06450 | 370.4 | 0.06443 | 370.3 |
| 25, 25 | 0.05 | 0.00787 | 369.8 | 0.01402 | 369.9 | 0.00821 | 370.4 | 0.01343 | 370.3 | 0.01497 | 369.8 | 0.01496 | 370.5 |
| | 0.10 | 0.01223 | 369.9 | 0.0218 | 370.0 | 0.01276 | 370.5 | 0.02087 | 369.0 | 0.02310 | 370.4 | 0.02309 | 369.5 |
| | 0.25 | 0.02162 | 370.6 | 0.03853 | 370.4 | 0.02255 | 370.1 | 0.0369 | 370.7 | 0.04059 | 370.2 | 0.04058 | 370.8 |
| 40, 25 | 0.05 | 0.00622 | 370.1 | 0.01109 | 369.9 | 0.00649 | 369.9 | 0.01062 | 370.5 | 0.01195 | 370.5 | 0.01194 | 370.2 |
| | 0.10 | 0.00967 | 369.3 | 0.01724 | 370.0 | 0.01009 | 370.6 | 0.01650 | 369.2 | 0.01847 | 369.7 | 0.01847 | 370.5 |
| | 0.25 | 0.01710 | 369.9 | 0.03048 | 370.7 | 0.01784 | 370.5 | 0.02918 | 370.4 | 0.03254 | 371.0 | 0.03252 | 369.8 |

NOTE: Designs of SOP charts ($\hat{\tau}, \hat{\kappa}, \tilde{\tau}, \tilde{\kappa}$) apply to any continuously distributed process. The table’s largest standard error for the ARL is 0.4.

4.1 In-control ARL Performance

Let us start with an investigation of chart design and ARL performance under the assumption “IC-iid”. As our novel EWMA SOP-charts in (7) are non-parametric, it suffices to focus on one particular kind of continuous distribution for the $Y_s^{(t)}$ for computing IC-ARLs and for determining the chart design—an obvious choice is the standard normal distribution $N(0, 1)$. Here, chart design means computing the CL parameter $l_{\cdot, \lambda}$ for the considered kind of control chart, for the selected value of λ , and the chosen target ARL_0 . Following the common practice in SPM, we focus on the target $ARL_0 \approx 370$. For the smoothing parameter λ , we choose the levels $\lambda \in \{0.25, 0.10, 0.05\}$ like in Weiß and Testik (2023), which corresponds to an increasing memory of the EWMA charts, ranging from a “medium” up to a “very strong” level. In our OOC-analyses in Section 4.2, however, we only focus on the “compromise choice” $\lambda = 0.10$ (strong memory) to keep the amount of simulations manageable. Furthermore, we did not consider larger values of λ (in particular, we did not consider the Shewhart case $\lambda = 1$) because the sample sizes m, n are often rather small

in quality applications (such as the bottle thickness in Example 2.1) such that the frequency vectors \hat{p}_t used for (6) are highly discrete. In our simulations, we focus on the sample sizes $(m, n) \in \{(10, 10), (15, 15), (25, 25), (40, 25)\}$ like in Weiß and Kim (2024), but we also briefly discuss the case $m = n = 1$ later in Remark 4.1.1. While the IC-simulations for the EWMA SOP-charts (7) can be restricted to i. i. d. $Y_s^{(t)} \sim N(0, 1)$ thanks to their non-parametric nature, the competing $\hat{\rho}$ -chart relies on a parametric statistic such that an individual chart design is necessary for each specific IC-marginal distribution. Therefore, in view of the OOC-scenarios considered in Section 4.2 below, the $\hat{\rho}$ -chart was also designed for i. i. d. Poisson data with mean 5, i. e., $Y_s^{(t)} \sim \text{Poi}(5)$. The obtained results are summarized in Table 1.

Table 2: IC-ARLs of EWMA $\hat{\rho}$ -charts with $\lambda = 0.1$ and target $\text{ARL}_0 \approx 370$, for different m, n combinations and different marginal distributions, but using the $N(0, 1)$ -CLs from Table 1; simulated with 10^5 replications.

| m, n | t(2) | BPoi | Wei | Exp | Poi | Lap | SkN | U | MixN | Ber |
|--------|--------|--------|--------|--------|--------|--------|--------|--------|--------|--------|
| 10, 10 | 590.76 | 514.94 | 465.06 | 464.82 | 410.59 | 392.42 | 389.60 | 357.43 | 352.20 | 349.14 |
| 15, 15 | 525.78 | 429.13 | 418.39 | 417.40 | 391.38 | 383.36 | 377.54 | 364.85 | 360.10 | 360.17 |
| 25, 25 | 457.68 | 392.11 | 390.43 | 389.41 | 380.83 | 374.48 | 374.69 | 368.64 | 365.42 | 366.65 |
| 40, 25 | 433.12 | 382.04 | 380.19 | 383.35 | 376.12 | 373.13 | 371.13 | 368.55 | 367.40 | 366.57 |

NOTE: The table’s largest standard error for the ARL is 1.84. Abbreviations used for column headings: BPoi = $\text{Ber}(0.2) \cdot \text{Poi}(5)$; Wei = $\text{Weibull}(1, 1.5)$, Exp = $\text{Exp}(1)$, Poi = $\text{Poi}(0.5)$, Lap = $\text{Laplace}(0, 1)$, SkN = $\text{SkewN}(0, 1, 10)$, U = $\text{U}(0, 1)$, MixN = $0.5 N(-9, 1) + 0.5 N(9, 1)$, Ber = $\text{Bernoulli}(0.5)$.

The designs of the EWMA SOP charts in Table 1 can be immediately used together with any continuously distributed DGP ($Y_s^{(t)}$) (or randomized integer DGP ($X_s^{(t)}$)). In particular, no prior Phase-I analysis is necessary, i. e., no model fitting to historical IC-data. Quite the contrary, the EWMA SOP charts could even be applied within Phase I for a retrospective data analysis. For the parametric $\hat{\rho}$ -chart, tailor-made chart designs after prior Phase-I analysis are necessary. Comparing the CLs for $N(0, 1)$ and $\text{Poi}(5)$ in Table 1, one might certainly get the impression that their differences are negligible. Moreover, we observed in simulation experiments that the $N(0, 1)$ -CLs are somehow robust: if the shape of the true IC-distribution is close to normal, then the IC-ARL obtained by using the $N(0, 1)$ -CLs is reasonably close to the target $\text{ARL}_0 \approx 370$. The same holds if the sample sizes m, n are sufficiently large, as the central limit theorem implies an asymptotic normal distribution for $\hat{\rho}(1)$. However, if the shape clearly deviates from normality and the sample sizes are small, using the $N(0, 1)$ -CLs might result in a misleading IC-ARL performance. This is illustrated by Table 2, where various different marginal distributions are considered for the i. i. d. DGP. For the smallest considered sample size, $(m, n) = (10, 10)$, the true IC-ARLs vary considerably, from about 349.14 up to 590.76. Analogous variations, though dampened, are observed for larger sample size (m, n) . In particular, depending on the actual marginal distribution, it might happen that the EWMA $\hat{\rho}$ -chart produces too many false alarms or is very conservative, where the latter causes a deterioration in OOC-performance. More precisely, for skewed distributions or distributions with heavier tails than the normal, we observe moderately to severely increased IC-ARLs, whereas platykurtic distributions (we selected examples from Westfall (2014, Table 1)) led to a decrease of the IC-ARL. Altogether, it becomes clear that the pronounced parametric nature of the EWMA $\hat{\rho}$ -chart requires a careful Phase-I analysis in practice, where an appropriate marginal distribution must be identified and fitted to the historical IC data. By contrast, as highlighted before, the non-parametric EWMA SOP charts can be applied immediately from the beginning of process monitoring.

Table 3: Clay flats at times $t = 1, \dots, 6$ according to Table 1 in [Barton and Gonzalez-Barreto \(1996\)](#): step-wise computation of EWMA-smoothed type frequencies $\hat{\boldsymbol{p}}_t^{(\lambda)}$ according to (6) with $\lambda = 0.1$ and $\boldsymbol{p}_0 = (\frac{1}{3}, \frac{1}{3}, \frac{1}{3})^\top$, where $(y_s^{(t)})$ comprises the four registration errors of the t th clay flat.

| | | | | | | |
|--------------------------------------|--|--|--|--|--|--|
| $(y_s^{(t)})$ | $\begin{pmatrix} 3.30 & 3.95 \\ 5.89 & 3.20 \end{pmatrix}$ | $\begin{pmatrix} 0.27 & 3.71 \\ 0.39 & 4.33 \end{pmatrix}$ | $\begin{pmatrix} 3.06 & 1.66 \\ 2.93 & 2.12 \end{pmatrix}$ | $\begin{pmatrix} 2.74 & 2.86 \\ 1.31 & 2.10 \end{pmatrix}$ | $\begin{pmatrix} 1.36 & 3.42 \\ 2.21 & 1.80 \end{pmatrix}$ | $\begin{pmatrix} 2.00 & 2.44 \\ 3.65 & 1.64 \end{pmatrix}$ |
| $\boldsymbol{\pi}_t$ | $\begin{pmatrix} 2 & 3 \\ 4 & 1 \end{pmatrix}$ | $\begin{pmatrix} 1 & 3 \\ 2 & 4 \end{pmatrix}$ | $\begin{pmatrix} 4 & 1 \\ 3 & 2 \end{pmatrix}$ | $\begin{pmatrix} 3 & 4 \\ 1 & 2 \end{pmatrix}$ | $\begin{pmatrix} 1 & 4 \\ 3 & 2 \end{pmatrix}$ | $\begin{pmatrix} 2 & 3 \\ 4 & 1 \end{pmatrix}$ |
| Type | 3 | 1 | 2 | 1 | 3 | 3 |
| $\hat{\boldsymbol{p}}_t$ | $\begin{pmatrix} 0 \\ 0 \\ 1 \end{pmatrix}$ | $\begin{pmatrix} 1 \\ 0 \\ 0 \end{pmatrix}$ | $\begin{pmatrix} 0 \\ 1 \\ 0 \end{pmatrix}$ | $\begin{pmatrix} 1 \\ 0 \\ 0 \end{pmatrix}$ | $\begin{pmatrix} 0 \\ 0 \\ 1 \end{pmatrix}$ | $\begin{pmatrix} 0 \\ 0 \\ 1 \end{pmatrix}$ |
| $\hat{\boldsymbol{p}}_t^{(\lambda)}$ | $\begin{pmatrix} 0.300 \\ 0.300 \\ 0.400 \end{pmatrix}$ | $\begin{pmatrix} 0.370 \\ 0.270 \\ 0.360 \end{pmatrix}$ | $\begin{pmatrix} 0.333 \\ 0.343 \\ 0.324 \end{pmatrix}$ | $\begin{pmatrix} 0.400 \\ 0.309 \\ 0.292 \end{pmatrix}$ | $\begin{pmatrix} 0.360 \\ 0.278 \\ 0.362 \end{pmatrix}$ | $\begin{pmatrix} 0.324 \\ 0.250 \\ 0.426 \end{pmatrix}$ |

4.1.1 Remark It should be noted that the SOP-EWMA charts are well defined already for $m = n = 1$ (provided that λ is clearly smaller than 1 to ensure a reasonable memory), i. e., if only one SOP is computed per rectangle. Such an application is described by [Barton and Gonzalez-Barreto \(1996\)](#), where a manufacturing process of multilayer chip capacitors is monitored. There, for each manufactured clay flat, the so-called registration error is determined for four pads (one from each quadrant), leading to a 2×2 measurement for each clay flat. This is illustrated by Table 3, where the 2×2 registration errors for the first six clay flats from Table 1 in [Barton and Gonzalez-Barreto \(1996\)](#) are shown in the first row, the corresponding SOPs in the second row, their types in the third row, the raw frequency vectors $\hat{\boldsymbol{p}}_t$ in the fourth row, and their EWMA-smoothed counterparts $\hat{\boldsymbol{p}}_t^{(\lambda)}$ in the last row. While the $\hat{\boldsymbol{p}}_t$ can take one out of only three possible values and are, thus, not suitable for defining a (Shewhart) control chart, the $\hat{\boldsymbol{p}}_t^{(\lambda)}$ can be used for the control charts in (7) despite the small sample size $m = n = 1$ —at least theoretically. While we were able to determine the IC-designs, see Table 1, the OOC-simulations showed that the OOC-ARLs decrease only very slowly for increasing deviation from the “IC-iid” assumption such that one has to expect large detection delays in practice. This is plausible in view of the low information content of a single 2×2 -SOP, and we decided to not further analyze the case $m = n = 1$.

4.2 Out-of-control ARL Performance

Let us now turn to an analysis of the OOC-ARL performance. Various spatially dependent DGPs for the rectangular sets $(Y_s^{(t)})_s$ are considered, in analogy to the power analyses in [Weiß and Kim \(2024\)](#). We begin our analyses with the most well-known case, unilateral SAR DGPs. More precisely, we consider the continuously distributed unilateral SAR(1, 1) process (see [Pickard, 1980](#)) defined by

$$Y_{t_1, t_2} = \alpha_1 \cdot Y_{t_1-1, t_2} + \alpha_2 \cdot Y_{t_1, t_2-1} + \alpha_3 \cdot Y_{t_1-1, t_2-1} + \varepsilon_{t_1, t_2} \quad (9)$$

with i. i. d. innovations $\varepsilon_{t_1, t_2} \sim N(0, 1)$ on the one hand, and its integer counterpart, the SINAR(1, 1) process (see [Ghodsi et al., 2012](#)), on the other hand:

$$X_{t_1, t_2} = \alpha_1 \circ X_{t_1-1, t_2} + \alpha_2 \circ X_{t_1, t_2-1} + \alpha_3 \circ X_{t_1-1, t_2-1} + \epsilon_{t_1, t_2}, \quad (10)$$

with i. i. d. innovations $\epsilon_{t_1, t_2} \sim \text{Poi}(5)$. Here, “ \circ ” denotes the binomial thinning operator introduced by [Steutel and van Harn \(1979\)](#), constituting an integer-valued substitute of the ordinary multiplication “ \cdot ”. It is defined by requiring that $\alpha \circ X | X \sim \text{Bin}(X, \alpha)$, i. e., $\alpha \circ X$ is conditionally binomially distributed with $\alpha \in [0; 1)$. The obtained OOC-ARLs are summarized in Appendix A in Tables A.1 and A.2, respectively, with the minimal OOC-ARLs being highlighted by bold font. Not surprisingly, for such unilateral linear DGPs, the $\hat{\rho}$ -chart performs best without exception. Nevertheless,

also the EWMA SOP-charts have clearly reduced ARLs, where usually the $\tilde{\tau}$ -chart performs best (with lower OOC-ARL for increased α_1, α_2). Only for the model specification $(\alpha_1, \alpha_2, \alpha_3) = (0.2, 0.2, 0.5)$, where the “diagonal” AR parameter α_3 is particularly large, the $\tilde{\tau}$ -chart has a poor performance and the $\hat{\kappa}$ -chart does best among the SOP-charts. This might be explained from the definition of $\tilde{\tau}$ in (4), which solely focuses on type 3, where the maximal ranks occur along one of the diagonals. Type 3, however, does not distinguish if the maximal ranks occur along the main diagonal (as caused by large α_3) or the anti-diagonal (which rarely happens for a unilateral DGP with large α_3). Therefore, the $\tilde{\tau}$ -chart fails in detecting a large α_3 .

In practice, however, we are often confronted with more demanding situations where the DGP deviates from the simple, well-behaved first-order autoregressive process. As the first non-textbook scenario, let us consider the same SAR DGPs (9) and (10) as before, but with the resulting data being contaminated by additive outliers (AOs). More precisely, 10 % of the generated data were randomly selected and manipulated by a further summand. In the case of the continuously distributed SAR(1, 1) DGP (9), we either added the fixed contamination +10, or one of +10 or −10 with probability 0.5 each. For the discrete SINAR(1, 1) DGP (10), the contamination was randomly chosen from the Poi(25)-distribution. The resulting OOC-ARLs are summarized in Appendix A in Tables A.3 and A.4, respectively. Except for the parametrization $(\alpha_1, \alpha_2, \alpha_3) = (0.2, 0.2, 0.5)$ already discussed before, the $\hat{\rho}$ -chart performs considerably worse. In addition, for the small grid $(m, n) = (10, 10)$ and $(\alpha_1, \alpha_2, \alpha_3) = (0.1, 0.1, 0.1)$, the OOC-ARL of the $\hat{\rho}$ -chart is considerably larger than the IC-ARL. The SOP charts, in turn, are robust against the outliers (recall that SOPs consist of ranks) and outperform the $\hat{\rho}$ -chart. More precisely, except for $(\alpha_1, \alpha_2, \alpha_3) = (0.2, 0.2, 0.5)$, the $\tilde{\tau}$ -chart leads to the lowest OOC-ARLs in nearly any case.

In the discrete count case, we considered a further variation of the basic unilateral SINAR(1, 1) DGP (10): the recursive scheme used for data generation is the same as in (10), but the innovations ϵ_{t_1, t_2} are not Poisson-distributed anymore but follow a zero-inflated Poisson (ZIP) distribution instead. More precisely, $\epsilon_{t_1, t_2} \sim \text{ZIP}(0.9, 5)$ with mean 5 again, but the value 0.9 of the zero-inflation parameter implies that at least 90 % of the innovations are equal to zero. In contrast, the remaining truly positive counts cause positive shocks to the DGP. Since such positive shocks are usually followed by multiple zero innovations, the binomial thinnings in the SINAR(1, 1) recursion lead to decaying count values. Altogether, the generated spatial dependence is combined with many zeros and decaying cascades of counts. The resulting OOC-ARLs are summarized in Table A.5 in Appendix A. It can be seen that the $\hat{\rho}$ -chart quickly recognizes the apparent spatial dependence. However, the $\tilde{\tau}$ -chart has—with the exception $(\alpha_1, \alpha_2, \alpha_3) = (0.2, 0.2, 0.5)$ —mostly similar or lower OOC-ARLs. Also, the $\hat{\tau}$ -chart performs comparatively well in this scenario.

Up to now, we only considered linear (unilateral) DGPs, although sometimes under “demanding conditions”, recall Tables A.3–A.5. Next, we investigate truly non-linear (unilateral) DGPs, namely the two kinds of quadratic moving average (QMA) process proposed by [Weiß and Kim \(2024\)](#). The continuously distributed version, the unilateral SQMA(1, 1) process, is defined by

$$Y_{t_1, t_2} = \beta_1 \cdot \epsilon_{t_1-1, t_2}^a + \beta_2 \cdot \epsilon_{t_1, t_2-1}^b + \beta_3 \cdot \epsilon_{t_1-1, t_2-1}^c + \epsilon_{t_1, t_2} \quad (11)$$

with i. i. d. innovations $\epsilon_{t_1, t_2} \sim \text{N}(0, 1)$. DGP (11) has powers $a, b, c \in \{1, 2\}$, so the MA-terms are either linear or squared. In our simulations, we considered the following four combinations for (a, b, c) : the combination (2, 2, 2) expresses that all MA-terms are squared, (2, 1, 2) that the β_1 - and β_3 -term are squared, (1, 1, 2) that only the β_3 -term is squared, and (2, 1, 1) that only the β_1 -term is squared, also see Table A.6 in Appendix A. The integer counterpart to (11) is the SQINMA(1, 1) process with i. i. d. Poi(5)-innovations ϵ_{t_1, t_2} , where

$$X_{t_1, t_2} = \beta_1 \circ \epsilon_{t_1-1, t_2}^a + \beta_2 \circ \epsilon_{t_1, t_2-1}^b + \beta_3 \circ \epsilon_{t_1-1, t_2-1}^c + \epsilon_{t_1, t_2}. \quad (12)$$

In Appendix A, Table A.7, we consider the same combinations for $(a, b, c) \in \{1, 2\}^3$ as before. The OOC-ARLs in Tables A.6 and A.7 show that such non-linear spatial dependence is often best detected by using the $\tilde{\tau}$ -chart. Especially for the small sample size $(m, n) = (10, 10)$, the $\tilde{\tau}$ -chart can be faster than the $\hat{\rho}$ -chart by a factor up to 22. Note again that, similar to the SAR(1, 1) model with additive outliers, for the small grid $(m, n) = (10, 10)$ and $(a, b, c) = (1^2, 2^1, 3^1)$, the OOC-ARL of the $\hat{\rho}$ -chart is larger than the IC-ARL. In the few cases where the $\hat{\rho}$ -chart has the lowest OOC-ARLs, the $\tilde{\tau}$ -chart still does reasonably well, so using the $\tilde{\tau}$ -chart for uncovering QMA-like spatial dependence appears to be a good universal solution.

Finally, let us turn to (continuously distributed) bilateral DGPs. For unilateral DGPs, the observation Y_{t_1, t_2} is generated by observations and innovations with “time” indices $\leq t_1, t_2$ only (“past information”). Bilateral DGPs, in turn, also incorporate information from times $\geq t_1, t_2$ (“future information”). Although this might look artificial at first glance, the bilateral approach constitutes a parametrically parsimonious way of generating an intensified spatial dependence structure. According to Whittle’s representation theorem (Whittle, 1954), under mild conditions, any bilateral spatial DGP can be represented (at least approximately) by a unilateral DGP having the same spatial ACF. This unilateral counterpart, however, would need much more model parameters than the bilateral formulation. The first-order simultaneous AR (SAR(1)) model is defined by

$$Y_{t_1, t_2} = a_1 \cdot Y_{t_1-1, t_2} + a_2 \cdot Y_{t_1, t_2-1} + a_3 \cdot Y_{t_1, t_2+1} + a_4 \cdot Y_{t_1+1, t_2} + \varepsilon_{t_1, t_2}, \quad (13)$$

where ε_{t_1, t_2} are i. i. d. $N(0, 1)$. The resulting OOC-ARLs are summarized in Table A.8 with different parameter values for (a_1, a_2, a_3, a_4) . Table A.9 considers additional contamination by AOs of ± 5 . The results in both tables clearly show the superiority of the $\tilde{\tau}$ -chart in all scenarios. In two cases with the small grid $(m, n) = (10, 10)$, the OOC-ARL of the $\hat{\rho}$ -chart is again larger than the IC-ARL.

The DGP for Table A.10, in turn, is a bilateral counterpart to the SQMA(1, 1) model (11). The first-order simultaneous QMA (SQMA(1)) model is defined by

$$Y_{t_1, t_2} = b_1 \cdot \varepsilon_{t_1-1, t_2-1}^a + b_2 \cdot \varepsilon_{t_1+1, t_2-1}^b + b_3 \cdot \varepsilon_{t_1+1, t_2+1}^c + b_4 \cdot \varepsilon_{t_1-1, t_2+1}^d + \varepsilon_{t_1, t_2}, \quad (14)$$

with i. i. d. $\varepsilon_{t_1, t_2} \sim N(0, 1)$, where the powers a, b, c, d are again either chosen as 1 (linear term) or 2 (quadratic term). The considered combinations are $(2, 2, 2, 2)$, $(2, 1, 2, 1)$, and $(2, 2, 1, 1)$. Table A.10 shows the empirical results. In the first case (all error terms are squared), either the $\hat{\kappa}$ - or $\tilde{\kappa}$ -chart have the lowest OOC-ARLs (but $\tilde{\tau}$ does not much worse). In the other two cases, the $\tilde{\tau}$ -chart is again superior.

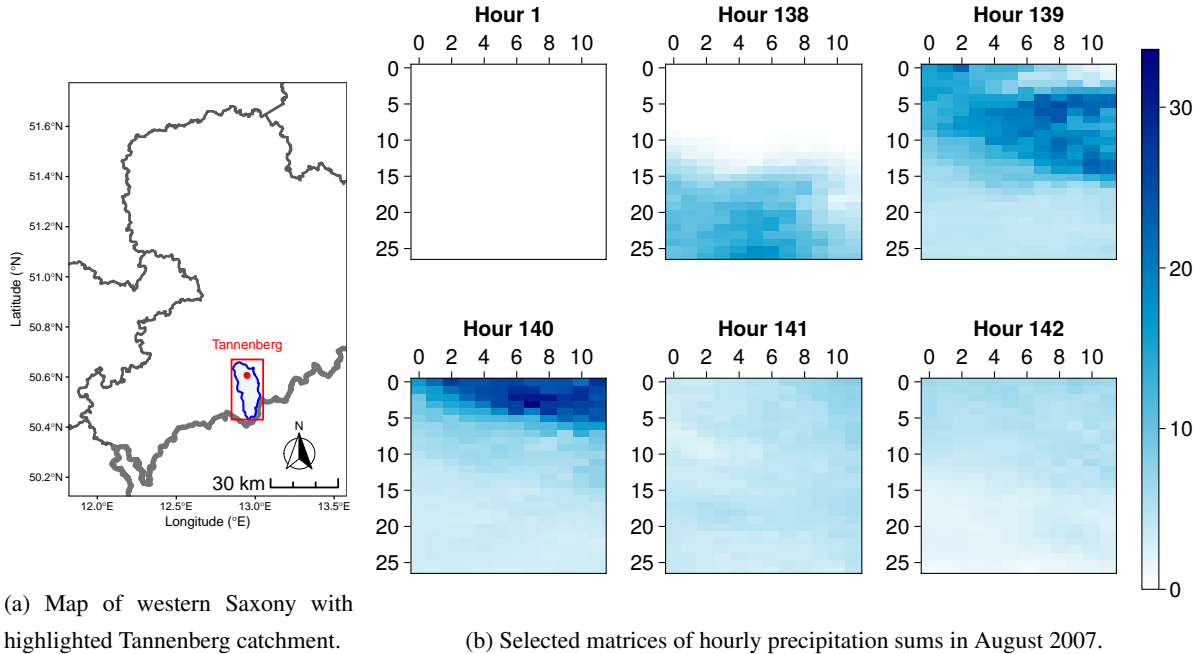
In a nutshell, we find, similar to Weiß and Kim (2024), that the $\tilde{\tau}$ -EWMA chart is a universally applicable solution to uncover the bilateral and non-linear spatial dependence. Therefore, it is our preferred choice for the real-data applications presented in the following Section 5.

5 Real-Data Applications

To illustrate the application of SOPs and types for monitoring streams of spatial grid data, we present three real-world data examples. Given the findings from the previous Section 4, we focus on the $\tilde{\tau}$ -EWMA chart for process monitoring. In the first two examples, we are concerned with discrete-valued grid data, namely rainfall data (Section 5.1) and counts of war-related fires in eastern Ukraine (Section 5.2). In both cases, the “IC-iid” assumption considered in Section 4 is adequate. The third application (Section 5.3) is more demanding in this respect. Here, we monitor (quasi-continuous) textile images, where we use a bootstrap approach to tailor the $\tilde{\tau}$ chart.

5.1 Rainfall data

As our first application, we consider the RADOLAN (“RADar-OnLine-ANeichung”) precipitation data set of Winterath et al. (2018), which provides reprocessed gauge-adjusted radar data expressing the one-hour precipitation sums (in 0.1 mm steps) in a $1 \text{ km} \times 1 \text{ km}$ grid. We focus on the Tannenberg catchment, located in the federal state of Saxony (Germany). This region is covered by the grid shown in Figure 2a (with $m = 26$ and $n = 11$). It was previously investigated by, among others, Fischer et al. (2024). According to Kaiser et al. (2021, Figure 9, p. 13), the Tannenberg catchment constitutes one of Germany’s hot spot regions for heavy rainfall-related flood events. Hence, applying a monitoring system for extraordinary precipitation events is of utmost practical importance.



(a) Map of western Saxony with highlighted Tannenberg catchment.

(b) Selected matrices of hourly precipitation sums in August 2007.

Figure 2: Map of the Tannenberg catchment in Germany with a rectangle grid of interest (left). Heat maps of hourly rainfall data for the Tannenberg catchment in August 2007. Grid sizes are $m = 26$ and $n = 11$.

To illustrate the application of the $\tilde{\tau}$ -EWMA chart, we consider the week between August 3–9, 2007, leading to 168 hourly observations. As we shall recognize below, two severe rain events occurred during this week; see also Figure 2b. Since our aim is to detect such severe rain events, the IC-model should refer to the situation of, at most, moderate precipitation. Then, however, ties are frequently observed, especially in times of no precipitation at all (like in “Hour 1” of Figure 2b). Hence, we apply the randomization approach (5) such that no-rain hours are transformed into i. i. d. uniform noise, satisfying the “IC-iid” assumption. Note that during hours with strong precipitation, the 0.1 mm steps are sufficiently fine such that ties hardly happen. Therefore, the randomization approach (5) has only little effect on the SOPs referring to such a case.

Figure 3a shows the resulting $\tilde{\tau}$ -EWMA chart with $\lambda = 0.1$, where $l_{\tilde{\tau},\lambda} = 0.0188204$ is calibrated for $ARL_0 = 370$ based on 10^6 IC-iid replications. The black sample path serves as our illustrative example since, in practice, one concentrates on one sequence of EWMA statistics. But to illustrate the possible consequences of the randomization approach (5), we indeed added 999 further runs (which are computed from the same data but using newly generated noise) as light-gray curves. The mean of the altogether 1000 runs is highlighted in blue, so it becomes clear that the

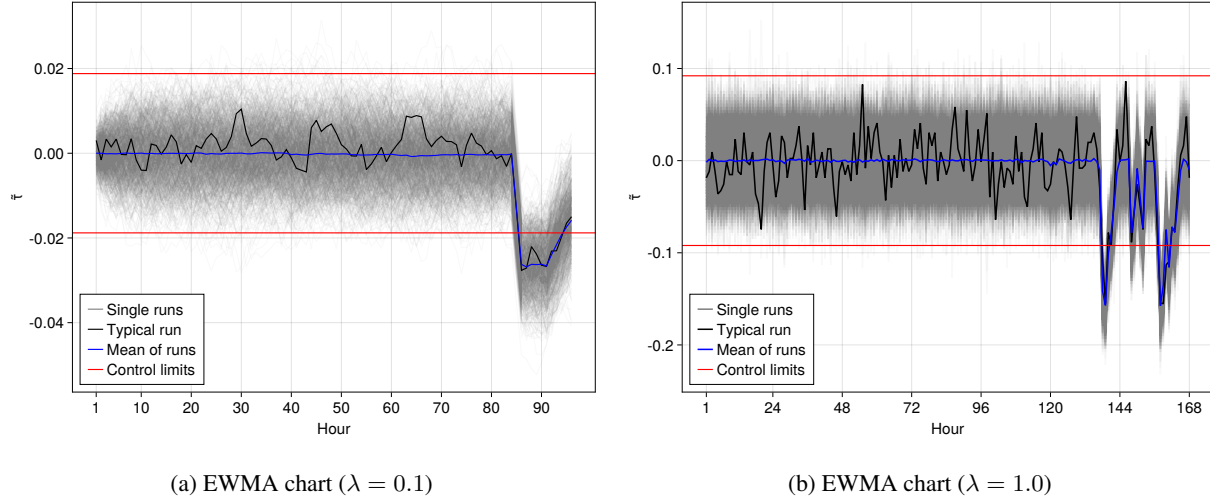


Figure 3: $\tilde{\tau}$ -charts with $\lambda = 0.1$ (left) and $\lambda = 1$ (right) of hourly rainfall data for the Tannenberg catchment in a single week interval 03/08/2007 - 09/08/2007. The light-gray curves show the control charts computed for 1000 single runs. Grid sizes are $m = 26$ and $n = 11$.

black line represents a “typical run”. Recall that the ARL computations already account for the randomization (as this is covered by the “IC-iid” assumption), i. e., any of the grey curves satisfies the IC-ARL target. This also gets clear from the first part of EWMA statistics (say, hours ≤ 100), where the process is IC and only a few gray curves lead to a (false) alarm ($ARL_0 = 370$ allows for a false alarm after 370 EWMA statistics in the mean).

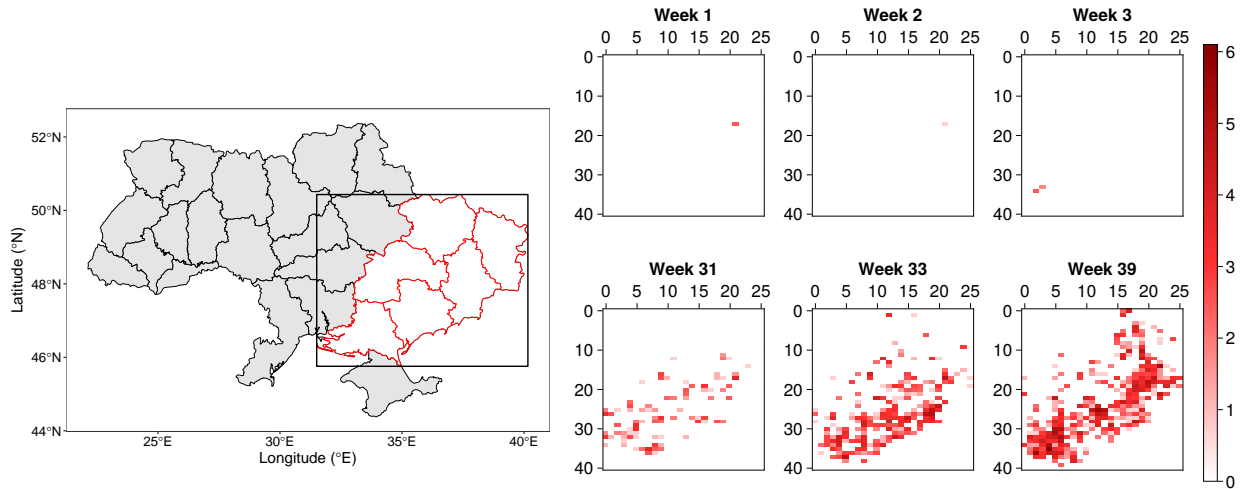
The first true alarms are triggered by the $\tilde{\tau}$ -EWMA chart at times ≥ 138 . At this point, it is useful to look at the $\tilde{\tau}$ -Shewhart chart (obtained by setting $\lambda = 1$, i. e., by removing any memory), which we added for the sake of interpretation in Figure 3b. Recall that we did not consider Shewhart charts in Section 4 as they are known to be insensitive to small process changes, and as they are difficult to design due to discreteness. In fact, it was not possible to meet $ARL_0 = 370$ precisely, but only $ARL_0 = 362.29$ for the control limit $l_{\tilde{\tau},\lambda} = 0.0920745$. Thus, Figure 3b mainly serves as a time series plot of the non-smoothed $\tilde{\tau}$ -statistics. It becomes clear that there seem to be two successive severe rain events, namely one around hours 138–140 (also see Figure 2b), and another around hours 158–161. Figure 3a shows that the first event is quickly detected by the $\tilde{\tau}$ -EWMA chart (with possibly slight delays depending on the actual noise). Due to its inherent memory, it continues to signal further alarms afterward. Then, the second event leads to a further drop-down of the EWMA-statistics (irrespective of the actual noise), i. e., both events are recognized by any of the $\tilde{\tau}$ -EWMA charts. At this point, it is worth noting that the second event also would have been detected at time 159 by our black curve if we would have re-initiated the EWMA chart after the first event (i. e., if we would have reset the EWMA statistics to 0 at time 139). So the $\tilde{\tau}$ -EWMA chart successfully uncovered the changes in spatial dependence caused by the abnormal precipitation behavior.

5.2 War-related fires in Ukraine

The Ukrainian-Russian war, which culminated in Russia’s full-scale invasion of Ukraine on the morning of 24 February 2022, is one of the most extensively documented wars in history (Myre, 2023). Especially at the beginning of the invasion, social media platforms were flooded with footage of airstrikes, first-hand accounts from bloggers embedded with military units, and updates on the ever-changing front lines. Despite the wealth of material available, however,

this documentation offers only a fragmented view as events that go unrecorded or unpublished remain obscured. By contrast, cameras positioned high above the battlefield offer a distinct advantage, providing a broader and alternative perspective on the ongoing war.

The British newspaper “The Economist” has monitored the war’s progression by utilizing the “Fire Information for Resource Management System” (FIRMS), a NASA program engineered to identify fires globally (The Economist and Solstad, 2023). In a nutshell, the authors use gradient-boosted trees from 10 non-war years in Ukraine to predict fires since the Russian invasion. If the true number of fires exceeds a certain predicted quantile, the fires are classified as war-related. The disadvantage of their approach is that FIRMS cannot detect fires through clouds. In addition, as the model is probabilistic, fires may be misclassified as war-related and vice versa. However, their data track the front lines exceptionally well, so we use their data as given and do not apply any post-processing. The data are publicly available on [GitHub](#) (accessed on April 12, 2024) and updated twice a day.



(a) Map of Ukraine with highlighted eastern regions.

(b) Selected count matrices of war-related fires in 2023.

Figure 4: Map of the Ukraine (left) highlighting the eastern Ukraine region by red outlines. The rectangle is our grid of interest. The right panel shows chosen weekly heatmaps of fires (log-scale) with grid sizes $m = 40$ and $n = 25$ (right).

We focus on the weekly numbers of war-related fires in 2023 and in the eastern provinces of Ukraine, where most of the fighting has been taking place, namely Luhanska, Dnipropetrovska, Donetska, Zaporizka, Kharkivska, and Khersonska. The provinces are highlighted in red in the left panel of Figure 4. We divide our chosen rectangle into bins (41 for latitude and 26 for longitude) and count the number of fires that occurred during the corresponding week in 2023 for each bin.² The count matrix is used to compute the SOPs, resulting in a matrix with $m = 40$ rows and $n = 25$ columns, corresponding to one of the simulation scenarios in Section 4. The right panel of Figure 4 shows the calculated count matrix for different weeks for the beginning and middle of 2023. It can be seen that almost no war-related fires were detected in the early weeks of 2023, which is most likely because FIRMS cannot detect fires through clouds. As the monitored data are discrete counts, we again use the randomization approach in (5). As a consequence, in weeks with no war-related fires, the SOPs are computed from pure uniform noise (also recall the data example from Section 5.1), which perfectly agrees with the “IC-iid” assumption considered in Section 3. By contrast,

²In total, the data contains 47,646 war-related fires for eastern Ukraine in 2023.

in weeks with a pronounced spatial pattern of fire activity (such as week 39 in Figure 4), we expect violations of the “IC-iid” assumption as the effect of the noise for SOP computation then largely fizzles out.

Figure 5 (a) shows the resulting $\tilde{\tau}$ -EWMA chart with $\lambda = 0.1$, the chart design of which is chosen according to Table 1. While the EWMA statistics are centered around zero in the first weeks of 2023, we observe a decreasing trend starting in March, culminating in several alarms for the weeks ≥ 35 (August/September 2023). This increasing activity in war-related fires can also be recognized from the lower panel of Figure 4 (b). At this point, it is also important to consider the corresponding Shewhart chart shown in Figure 5 (b). Although it does not lead to any alarm, we recognize a phase with slightly negative $\tilde{\tau}$ -values roughly between weeks 30 and 40. As we are concerned with only mild violations of the $\tilde{\tau}$ ’s IC-value 0, the EWMA chart’s inherent memory clearly turns out to be beneficial for monitoring war-related fires. Recalling the definition of $\tilde{\tau}$ according to (4), negative values of $\tilde{\tau}$ indicate that type 3 occurs less frequently than expected under IC-assumptions, i. e., the highest ranks tend to occur (slightly) more often along rows or columns rather than on a diagonal. Such “dominant rows or columns” can also be recognized in Figure 4 (b), which constitute themselves as horizontal or vertical stripes within the grid.

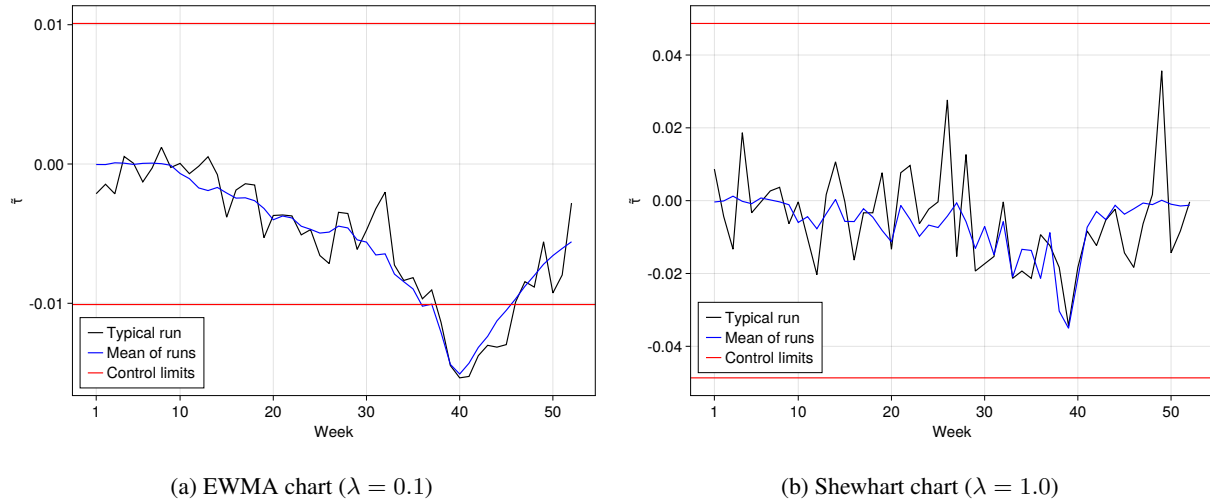


Figure 5: $\tilde{\tau}$ -charts with $\lambda = 0.1$ (left) and $\lambda = 1.0$ (right) applied to data on war-related fires in east Ukraine (see Figure 4) for the year 2023 (black curve). Grid sizes are $m = 40$ and $n = 25$. The blue curve is the average chart computed across 1000 charts.

5.3 Textile images

Our last real-data example considers the monitoring of textile images, which are provided by the R-package `textile` and further described in Bui and Apley (2018). More precisely, 100 images with resolution 250×250 (so $m = n = 249$) are available, where the first 94 are without local defects according to Bui and Apley (2018) while the last six images are affected by different issues such as fiber direction changes, tears, or holes. Strictly speaking, we are again concerned with discrete-valued data as the available images of textile material are plotted on a grey scale with levels from 0 (black) to 255 (white). However, as the range is rather large (“quasi-continuous”), ties within 2×2 squares are not that frequent such that a prior randomization is omitted this time.

To monitor the sequence of textile images, we first start with the “default IC-model” again, namely the “IC-iid” assumption. Since the sample size $m = n = 249$ is not covered by Table 1, we first have to determine the chart

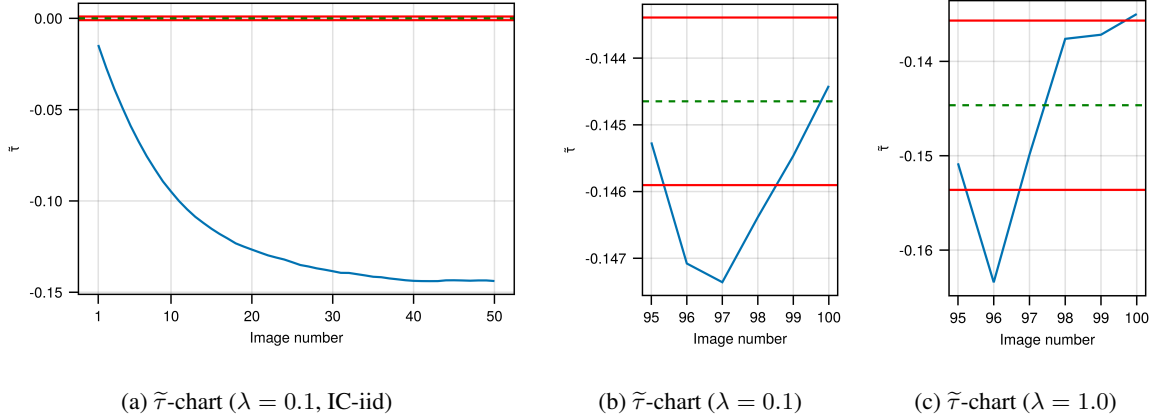


Figure 6: $\tilde{\tau}$ -EWMA chart with $\lambda = 0.1$ and $ARL_0 \approx 100$ under “IC-iid” assumption in (a). $\tilde{\tau}$ -charts for OOC data with (b) $\lambda = 0.1$ and (c) $\lambda = 1$, using resampling approach with $ARL_0 \approx 20$. Grid sizes are $m = n = 249$.

design for the intended $\tilde{\tau}$ -EWMA chart with $\lambda = 0.1$. In view of having only 100 images available in the R-package `textile`, we set the IC-target to $ARL_0 = 100$, leading to the control limit $l_{\tilde{\tau},\lambda} = 0.0010174$. Figure 6a shows the resulting $\tilde{\tau}$ -EWMA chart for the first 50 observations. It is clearly visible that the “IC-iid” assumption for the control chart does not hold. This is plausible given the regular spatial structure of the textile images; see Patch 1 in Figure 7 as an example, which implies a particular form of spatial dependence. However, it is not clear with which kind of stochastic model the apparent spatial dependence can be described.

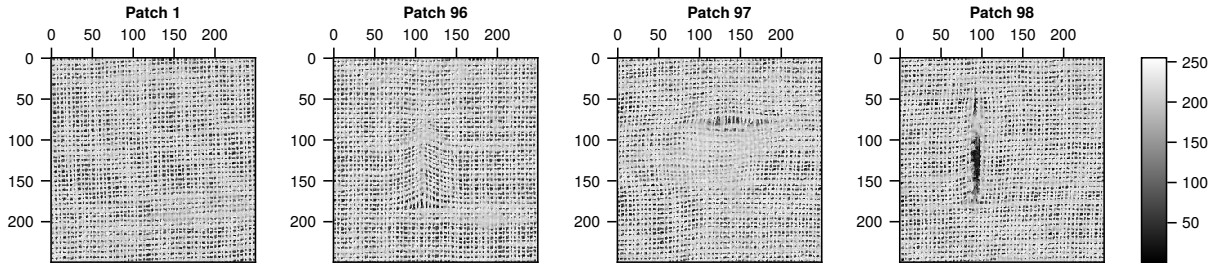


Figure 7: Textile images from IC-sample (Patch 1) and OOC-sample (Patches 96–98) with grid sizes are $m = n = 249$. The local defects are a fiber direction change (96), a tear (97), and a hole (98), see [Bui and Apley \(2018, Figure 8\)](#).

Thus, to still apply the $\tilde{\tau}$ -EWMA chart to the data, we utilize a kind of Efron bootstrap approach. Here, we use the 96 IC-observations as the Phase-I data for resampling, the IC-mean of which equals ≈ -0.145 (instead of 0 as under the “IC-iid” assumption). Note that negative $\tilde{\tau}$ -values imply that the maximal ranks mainly occur along rows and columns, which is plausible because of the vertical and horizontal fiber directions. According to our bootstrap approach, we sequentially resample from the 96 IC-values of $\tilde{\tau}$, apply the $\tilde{\tau}$ -EWMA chart (initialized with the IC-mean) to the resulting image sequence, and determine the respective run length. ARLs are then computed based on 10^6 replications again. Since the R-package `textile` provides only six OOC-images for Phase II, we set the IC-target to $ARL_0 = 20$, leading to the control limit $l_{\tilde{\tau},\lambda} = 0.0012559$. The application of the $\tilde{\tau}$ -EWMA chart with $\lambda = 0.1$ to the Phase-II data is shown in Figure 6b. It triggers an alarm for Patches 96, 97, and 98, showing different local defects; see Figure 7. For interpretation, we also show the raw $\tilde{\tau}$ -values in the form of a Shewhart chart; see Figure 6c. Its control limit is

$l_{\tilde{\tau},\lambda} = 0.0089714$, leading to $ARL_0 \approx 18.8$ (note that due to the limited amount of Phase-I data, the IC-target ARL can only be met approximately for the Shewhart chart). It can be seen that Patch 96 leads to a particularly strong negative value, i. e., the maximal ranks occur even rarer along the diagonals. This is probably explained by the long vertical fibers below the fiber direction change; see Figure 7. Altogether, the $\tilde{\tau}$ -EWMA chart successfully detected the disturbances of the regular textile structure, which correspond to changes in spatial dependence.

6 Conclusions and Future Research

There is increasing attention to the monitoring of streams of rectangular data in the SPM literature. In this study, we considered data that were collected as a regular two-dimensional grid. To monitor such streams of data for possible spatial dependence, we proposed non-parametric control charts based on 2×2 -SOPs. It is assumed that the rectangular data sets originate from continuously-distributed RVs. However, for discrete RVs and limited measurement precision, a randomization approach was also proposed, as there may be ties in the rankings in the SOPs. It is further assumed that the rectangular sets are generated independently of each other for different t , but the RVs within the t th rectangular set can follow any joint distribution.

To construct the proposed control charts, the relative frequency vectors of the SOPs were used both solely to calculate the control statistics for the Shewhart-type control charts, which have no memory, and as an EWMA of the process of frequency vectors to develop control charts with inherent memory. We proposed four classes of control charts, each with a different control statistic.

Extensive performance evaluations were carried out using zero-state ARL simulations. In the OOC simulations, we used various spatially dependent DGPs—unilateral and bilateral, linear and non-linear, contaminated and non-contaminated, discrete and continuous—to evaluate the out-of-control ARL performance of the charts. As a natural competitor to our SOP-based charts, analogous charts on the basis of spatial ACF were also considered. Note that the ACF approach is parametric in nature, so the chart design requires a full specification of the in-control model. In contrast, SOP chart designs can be used immediately with any continuously distributed DGP. In particular, no prior Phase-I analysis is necessary, but these charts could even be applied within Phase-I for a retrospective data analysis. We found that the $\tilde{\tau}$ chart was generally the superior chart, and in those cases where another chart was optimal, the $\tilde{\tau}$ chart performed similarly well. Hence, the $\tilde{\tau}$ -EWMA chart constitutes a universally applicable solution to uncover spatial dependence. Finally, three real-world cases were used to illustrate the applicability and effectiveness of the proposed method, namely heavy rainfall in Germany, war-related fires in eastern Ukraine, and manufacturing defects in textile production.

There are various related directions for future research. For example, we used the types proposed by [Bandt and Wittfeld \(2023\)](#) for defining our control charts. Distinguishing three types only, however, constitutes a rather rough discretization of the original data, which may result in information loss. Therefore, we recommend developing “refined types” (i.e. a finer partitioning of the set of SOPs) and the corresponding control charts, and analysing whether these lead to improved detection performance for some OOC scenarios. Another direction is inspired by the discreteness of data often observed in real applications (recall those discussed in Section 5). Our current solution is to add uniform noise to integer data to break ties, particularly useful in situations where constant rectangles might be observed under IC conditions (e. g., no precipitation or no fires at all, recall Section 5). In other applications, however, ties may contain valuable information about the actual spatial dependence structure, which is obviously lost after noise is added. In

such cases, the concept of generalized OPs from Weiß and Schnurr (2024) might be useful. It should be analyzed whether a feasible definition of “generalized SOPs” is possible and how corresponding control charts work in practice.

Data

The war-related fire data are available at <https://github.com/TheEconomist/the-economist-war-fire-model>. The Radolan rain data are available at https://opendata.dwd.de/climate_environment/CDC/grids_germany/hourly/radolan/. The images of textile material are available in the R-package `textile` (Bui and Apley, 2018).

Software

We used the programming language Julia (Bezanson et al., 2017) for the simulations and analyses and the package Makie (Danisch and Krumbiegel, 2021) for the visualizations.

Acknowledgements

The authors are grateful to Professor Scott D. Grimshaw (Brigham Young University) for providing the bottle thickness data discussed in Example 2.1. The authors would like to thank Dr. Svenja Fischer (Wageningen University) and Professor Alexander Schnurr (University of Siegen) for providing details of the Radolan rain data. The authors are also grateful to Dr. Sondre Solstad (The Economist) for an insightful discussion of the construction and intricacies of tracking war-related fires in Ukraine.

References

- C. Bandt. Small order patterns in big time series: A practical guide. *Entropy*, 21(6):613, 2019. doi:10.3390/e21060613.
- C. Bandt. Statistics and contrasts of order patterns in univariate time series. *Chaos: An Interdisciplinary Journal of Nonlinear Science*, 33(3):033124, 2023. doi:10.1063/5.0132602.
- C. Bandt and B. Pompe. Permutation entropy: A natural complexity measure for time series. *Physical Review Letters*, 88(17):174102, 2002. doi:10.1103/physrevlett.88.174102.
- C. Bandt and K. Wittfeld. Two new parameters for the ordinal analysis of images. *Chaos: An Interdisciplinary Journal of Nonlinear Science*, 33(4):043124, 04 2023. doi:10.1063/5.0136912.
- R. R. Barton and D. R. Gonzalez-Barreto. Process-oriented basis representations for multivariate process diagnostics. *Quality Engineering*, 9(1):107–118, 1996. doi:10.1080/08982119608919022.
- J. Bezanson, A. Edelman, S. Karpinski, and V. B. Shah. Julia: A fresh approach to numerical computing. *SIAM Review*, 59(1):65–98, 2017. doi:10.1137/141000671.
- A. T. Bui and D. W. Apley. A monitoring and diagnostic approach for stochastic textured surfaces. *Technometrics*, 60: 1–13, 2018. doi:10.1080/00401706.2017.1302362.
- B. M. Colosimo. Modeling and monitoring methods for spatial and image data. *Quality Engineering*, 30(1):94–111, 2018. doi:10.1080/08982112.2017.1366512.
- T. Czimmermann, G. Ciuti, M. Milazzo, M. Chiurazzi, S. Roccella, C. M. Oddo, and P. Dario. Visual-based defect detection and classification approaches for industrial applications—a survey. *Sensors*, 20(5), 2020. doi:10.3390/s20051459.

- S. Danisch and J. Krumbiegel. Makie. jl: Flexible high-performance data visualization for julia. *Journal of Open Source Software*, 6(65):3349, 2021. doi:[10.21105/joss.03349](https://doi.org/10.21105/joss.03349).
- S. Fischer, M. Oesting, and A. Schnurr. Multivariate motion patterns and applications to rainfall radar data. *Stochastic Environmental Research and Risk Assessment*, 38:1235–1249, 2024. doi:[10.1007/s00477-023-02626-7](https://doi.org/10.1007/s00477-023-02626-7).
- A. Ghodsi, M. Shitan, and H. S. Bakouch. A first-order spatial integer-valued autoregressive sinar(1, 1) model. *Communications in Statistics - Theory and Methods*, 41(15):2773–2787, 2012. doi:[10.1080/03610926.2011.560739](https://doi.org/10.1080/03610926.2011.560739).
- S. D. Grimshaw, N. J. Blades, and M. P. Miles. Spatial control charts for the mean. *Journal of Quality Technology*, 45(2):130–148, 2013. doi:[10.1080/00224065.2013.11917922](https://doi.org/10.1080/00224065.2013.11917922).
- W. Jiang, S. W. Han, K.-L. Tsui, and W. H. Woodall. Spatiotemporal surveillance methods in the presence of spatial correlation. *Statistics in Medicine*, 30(5):569–583, 2011. doi:[10.1002/sim.3877](https://doi.org/10.1002/sim.3877).
- M. Kaiser, S. Günemann, and M. Disse. Spatiotemporal analysis of heavy rain-induced flood occurrences in germany using a novel event database approach. *Journal of Hydrology*, 595:125985, 2021. doi:[10.1016/j.jhydrol.2021.125985](https://doi.org/10.1016/j.jhydrol.2021.125985).
- S. Knoth. The art of evaluating monitoring schemes — how to measure the performance of control charts? In *Frontiers in Statistical Quality Control 8*, pages 74–99. Physica-Verlag, 2006. doi:[10.1007/3-7908-1687-6_5](https://doi.org/10.1007/3-7908-1687-6_5).
- J. A. F. Machado and J. M. C. S. Silva. Quantiles for counts. *Journal of the American Statistical Association*, 100(472):1226–1237, 2005. doi:[10.1198/016214505000000330](https://doi.org/10.1198/016214505000000330).
- F. M. Megahed, W. H. Woodall, and J. A. Camelio. A review and perspective on control charting with image data. *Journal of Quality Technology*, 43(2):83–98, 2011. doi:[10.1080/00224065.2011.11917848](https://doi.org/10.1080/00224065.2011.11917848).
- F. M. Megahed, L. J. Wells, J. A. Camelio, and W. H. Woodall. A spatiotemporal method for the monitoring of image data. *Quality and Reliability Engineering International*, 28(8):967–980, 2012. doi:[10.1002/qre.1287](https://doi.org/10.1002/qre.1287).
- M. Meyer, C. Jentsch, and J.-P. Kreiss. Baxter’s inequality and sieve bootstrap for random fields. *Bernoulli*, 23(4B):2988 – 3020, 2017. doi:[10.3150/16-BEJ835](https://doi.org/10.3150/16-BEJ835).
- D. C. Montgomery. *Statistical quality control: a modern introduction*. John Wiley & Sons, Inc, New York., 6th edition, 2009.
- G. Myre. From drone videos to selfies at the front, ukraine is the most documented war ever. *National Public Radio*, 2023. URL <https://www.npr.org/2023/08/02/1191557426/ukraine-war-news-coverage>.
- P. S. Olmstead. Our debt to walter shewhart. *Industrial Quality Control*, 24(2):72–73, 1967.
- D. K. Pickard. Unilateral markov fields. *Advances in Applied Probability*, 12(3):655–671, 1980. doi:[10.2307/1426425](https://doi.org/10.2307/1426425).
- H. V. Ribeiro, L. Zunino, E. K. Lenzi, P. A. Santoro, and R. S. Mendes. Complexity-entropy causality plane as a complexity measure for two-dimensional patterns. *PLOS ONE*, 7(8):1–9, 08 2012. doi:[10.1371/journal.pone.0040689](https://doi.org/10.1371/journal.pone.0040689).
- S. W. Roberts. Control chart tests based on geometric moving averages. *Technometrics*, 1(3):239–250, 1959. doi:[10.1080/00401706.1959.10489860](https://doi.org/10.1080/00401706.1959.10489860).
- G. C. Runger and J. W. Fowler. Run-to-run control charts with contrasts. *Quality and Reliability Engineering International*, 14(4):261–272, 1998. doi:[10.1002/\(SICI\)1099-1638\(199807/08\)14:4<261::AID-QRE192>3.0.CO;2-R](https://doi.org/10.1002/(SICI)1099-1638(199807/08)14:4<261::AID-QRE192>3.0.CO;2-R).
- F. Steutel and K. van Harn. Discrete analogues of self-decomposability and stability. *Annals of Probability*, 7(5):893–899, 1979. doi:[10.1214/aop/1176994950](https://doi.org/10.1214/aop/1176994950).

- The Economist and S. Solstad. The Economist war-fire model. First published in the article “A hail of destruction”. *The Economist*, 2023. URL <https://www.economist.com/interactive/briefing/2023/02/23/data-from-satellites-reveal-the-vast-extent-of-fighting-in-ukraine>.
- P. Tsiamyrtzis, M. L. G. Grasso, and B. M. Colosimo. Image based statistical process monitoring via partial first order stochastic dominance. *Quality Engineering*, 34(1):96–124, 2022. doi:10.1080/08982112.2021.2008974.
- K. Wang and F. Tsung. Using profile monitoring techniques for a data-rich environment with huge sample size. *Quality and Reliability Engineering International*, 21(7):677–688, 2005. doi:10.1002/qre.711.
- C. H. Weiß. Non-parametric tests for serial dependence in time series based on asymptotic implementations of ordinal-pattern statistics. *Chaos: An Interdisciplinary Journal of Nonlinear Science*, 32(9):093107, 2022. doi:10.1063/5.0094943.
- C. H. Weiß and H.-Y. Kim. Using spatial ordinal patterns for non-parametric testing of spatial dependence. *Spatial Statistics*, 59:100800, 2024. doi:10.1016/j.spasta.2023.100800.
- C. H. Weiß and A. Schnurr. Generalized ordinal patterns in discrete-valued time series: nonparametric testing for serial dependence. *Journal of Nonparametric Statistics*, 36(3):573–599, 2024. doi:10.1080/10485252.2023.2231565.
- C. H. Weiß and M. C. Testik. Nonparametric control charts for monitoring serial dependence based on ordinal patterns. *Technometrics*, 65(3):340–350, 2023. doi:10.1080/00401706.2022.2157883.
- P. Westfall. Kurtosis as peakedness, 1905–2014. R.I.P. *The American Statistician*, 68(3):191–195, 2014. doi:10.1080/00031305.2014.917055.
- P. Whittle. On stationary processes in the plane. *Biometrika*, 41(3/4):434–449, 1954. doi:10.1093/biomet/41.3-4.434.
- T. Winterrath, C. Brendel, M. Hafer, T. Junghänel, A. Klameth, K. Lengfeld, E. Walawender, E. Weigl, and A. Becker. RADKLIM Version 2017.002: Reprocessed gauge-adjusted radar data, one-hour precipitation sums (RW). Technical report, Deutscher Wetterdienst (DWD), 2018.

Appendix A Out-of-control ARL performance results

Table A.1: OOC-ARLs of EWMA SOP-charts and competing $\hat{\rho}$ -chart for unilateral SAR(1, 1) model, for different $m, n, \alpha_1, \alpha_2, \alpha_3$ combinations, smoothing parameter $\lambda = 0.1$, and target $ARL_0 \approx 370$; simulated with 10^5 replications.

| m, n | α_1 | α_2 | α_3 | $\hat{\tau}$ -chart | $\hat{\kappa}$ -chart | $\tilde{\tau}$ -chart | $\tilde{\kappa}$ -chart | $\hat{\rho}$ -chart |
|--------|------------|------------|------------|---------------------|-----------------------|-----------------------|-------------------------|---------------------|
| 10, 10 | 0.1 | 0.1 | 0.1 | 72.01 | 90.46 | 52.78 | 208.1 | 9.49 |
| 15, 15 | | | | 36.88 | 45.33 | 25.86 | 140.42 | 5.05 |
| 25, 25 | | | | 15.97 | 19.04 | 11.53 | 69.06 | 2.80 |
| 40, 25 | | | | 11.32 | 13.18 | 8.34 | 46.98 | 2.22 |
| 10, 10 | 0.2 | 0.2 | 0.2 | 19.38 | 28.96 | 15.52 | 66.94 | 3.16 |
| 15, 15 | | | | 10.6 | 14.78 | 8.63 | 34.85 | 2.06 |
| 25, 25 | | | | 5.51 | 7.25 | 4.62 | 15.42 | 1.13 |
| 40, 25 | | | | 4.22 | 5.45 | 3.59 | 10.97 | 1.0 |
| 10, 10 | 0.2 | 0.2 | 0.5 | 25.51 | 171.05 | 212.29 | 24.4 | 1.57 |
| 15, 15 | | | | 13.61 | 100.11 | 134.7 | 13.09 | 1.0 |
| 25, 25 | | | | 6.89 | 43.76 | 64.49 | 6.61 | 1.0 |
| 40, 25 | | | | 5.21 | 29.38 | 44.01 | 5.0 | 1.0 |
| 10, 10 | 0.4 | 0.3 | 0.1 | 5.05 | 6.90 | 4.33 | 13.03 | 2.47 |
| 15, 15 | | | | 3.27 | 4.29 | 2.86 | 7.57 | 1.63 |
| 25, 25 | | | | 2.07 | 2.55 | 1.96 | 4.17 | 1.0 |
| 40, 25 | | | | 1.81 | 2.09 | 1.56 | 3.26 | 1.0 |

NOTE: The table's largest standard error for the ARL is 0.64

Table A.2: OOC-ARLs of EWMA SOP-charts and competing $\hat{\rho}$ -chart for unilateral SINAR(1, 1) model, for different $m, n, \alpha_1, \alpha_2, \alpha_3$ combinations, smoothing parameter $\lambda = 0.1$, and target $ARL_0 \approx 370$; simulated with 10^5 replications.

| m, n | α_1 | α_2 | α_3 | $\hat{\tau}$ -chart | $\hat{\kappa}$ -chart | $\tilde{\tau}$ -chart | $\tilde{\kappa}$ -chart | $\hat{\rho}$ -chart |
|--------|------------|------------|------------|---------------------|-----------------------|-----------------------|-------------------------|---------------------|
| 10, 10 | 0.1 | 0.1 | 0.1 | 74.44 | 92.08 | 54.62 | 214.0 | 9.49 |
| 15, 15 | | | | 38.29 | 46.23 | 26.63 | 146.33 | 5.05 |
| 25, 25 | | | | 16.6 | 19.43 | 11.86 | 72.59 | 2.79 |
| 40, 25 | | | | 11.72 | 13.46 | 8.54 | 49.83 | 2.23 |
| 10, 10 | 0.2 | 0.2 | 0.2 | 19.83 | 29.25 | 15.77 | 70.03 | 3.16 |
| 15, 15 | | | | 10.82 | 14.93 | 8.73 | 36.2 | 2.06 |
| 25, 25 | | | | 5.62 | 7.3 | 4.68 | 16.02 | 1.13 |
| 40, 25 | | | | 4.31 | 5.48 | 3.63 | 11.37 | 1.0 |
| 10, 10 | 0.2 | 0.2 | 0.5 | 25.68 | 172.17 | 214.69 | 24.8 | 1.57 |
| 15, 15 | | | | 13.85 | 100.61 | 137.38 | 13.26 | 1.0 |
| 25, 25 | | | | 6.97 | 43.85 | 66.3 | 6.68 | 1.0 |
| 40, 25 | | | | 5.25 | 29.47 | 45.33 | 5.06 | 1.0 |
| 10, 10 | 0.4 | 0.3 | 0.1 | 5.12 | 6.92 | 4.35 | 13.32 | 2.47 |
| 15, 15 | | | | 3.3 | 4.3 | 2.88 | 7.71 | 1.63 |
| 25, 25 | | | | 2.08 | 2.56 | 1.97 | 4.22 | 1.0 |
| 40, 25 | | | | 1.83 | 2.09 | 1.58 | 3.31 | 1.0 |

NOTE: The table's largest standard error for the ARL is 0.65.

Table A.3: OOC-ARLs of EWMA SOP-charts and competing $\hat{\rho}$ -chart for unilateral SAR(1, 1) model like in Table A.1, smoothing parameter $\lambda = 0.1$, but where 10 % of observations contaminated by AOs; simulated with 10^5 replications.

| m, n | α_1 | α_2 | α_3 | c | $\hat{\tau}$ -chart | $\hat{\kappa}$ -chart | $\tilde{\tau}$ -chart | $\tilde{\kappa}$ -chart | $\hat{\rho}$ -chart |
|--------|------------|------------|------------|----------|---------------------|-----------------------|-----------------------|-------------------------|---------------------|
| 10, 10 | 0.1 | 0.1 | 0.1 | 10 | 149.34 | 123.08 | 90.48 | 323.06 | 463.76 |
| 15, 15 | | | | | 85.98 | 64.54 | 44.73 | 296.1 | 216.56 |
| 25, 25 | | | | | 37.45 | 26.75 | 18.63 | 234.09 | 76.89 |
| 40, 25 | | | | | 25.16 | 18.21 | 12.97 | 195.44 | 47.65 |
| 10, 10 | 0.2 | 0.2 | 0.2 | 10 | 44.94 | 40.8 | 26.04 | 201.65 | 96.28 |
| 15, 15 | | | | | 22.93 | 20.31 | 13.51 | 135.47 | 33.41 |
| 25, 25 | | | | | 10.55 | 9.43 | 6.72 | 66.61 | 12.32 |
| 40, 25 | | | | | 7.7 | 6.94 | 5.07 | 45.59 | 8.6 |
| 10, 10 | 0.2 | 0.2 | 0.5 | 10 | 52.1 | 277.17 | 299.35 | 51.02 | 9.22 |
| 15, 15 | | | | | 26.56 | 197.52 | 212.28 | 25.84 | 4.8 |
| 25, 25 | | | | | 12.03 | 103.42 | 112.29 | 11.72 | 2.6 |
| 40, 25 | | | | | 8.69 | 71.33 | 78.24 | 8.49 | 2.09 |
| 10, 10 | 0.4 | 0.3 | 0.1 | 10 | 9.46 | 8.92 | 6.25 | 49.48 | 34.36 |
| 15, 15 | | | | | 5.69 | 5.37 | 3.95 | 26.32 | 12.95 |
| 25, 25 | | | | | 3.25 | 3.1 | 2.37 | 12.15 | 5.72 |
| 40, 25 | | | | | 2.58 | 2.46 | 2.01 | 8.83 | 4.25 |
| 10, 10 | 0.1 | 0.1 | 0.1 | ± 10 | 154.87 | 120.35 | 91.08 | 331.11 | 550.84 |
| 15, 15 | | | | | 90.59 | 63.2 | 44.44 | 307.85 | 273.57 |
| 25, 25 | | | | | 39.34 | 26.26 | 18.66 | 256.87 | 93.36 |
| 40, 25 | | | | | 26.34 | 17.85 | 13.02 | 221.77 | 57.19 |
| 10, 10 | 0.2 | 0.2 | 0.2 | ± 10 | 47.7 | 39.74 | 26.12 | 218.07 | 127.87 |
| 15, 15 | | | | | 24.01 | 19.86 | 13.51 | 153.42 | 39.92 |
| 25, 25 | | | | | 10.99 | 9.27 | 6.73 | 78.91 | 14.1 |
| 40, 25 | | | | | 7.99 | 6.82 | 5.09 | 54.49 | 9.73 |
| 10, 10 | 0.2 | 0.2 | 0.5 | ± 10 | 53.39 | 282.04 | 300.79 | 52.76 | 10.2 |
| 15, 15 | | | | | 27.13 | 204.26 | 213.11 | 26.54 | 5.27 |
| 25, 25 | | | | | 12.29 | 107.91 | 112.81 | 11.99 | 2.82 |
| 40, 25 | | | | | 8.89 | 74.71 | 78.47 | 8.69 | 2.23 |
| 10, 10 | 0.4 | 0.3 | 0.1 | ± 10 | 9.85 | 8.74 | 6.27 | 57.94 | 41.13 |
| 15, 15 | | | | | 5.88 | 5.28 | 3.95 | 30.91 | 14.73 |
| 25, 25 | | | | | 3.35 | 3.06 | 2.37 | 14.05 | 6.34 |
| 40, 25 | | | | | 2.66 | 2.43 | 2.01 | 10.1 | 4.69 |

NOTE: The table's largest standard error for the ARL is 1.72.

Table A.4: OOC-ARLs of EWMA SOP-charts and competing $\hat{\rho}$ -chart for unilateral SINAR(1, 1) model like in Table A.2, smoothing parameter $\lambda = 0.1$, but where 10 % of observations contaminated by AOs from Poi(25); simulated with 10^5 replications.

| m, n | α_1 | α_2 | α_3 | $\hat{\tau}$ -chart | $\hat{\kappa}$ -chart | $\tilde{\tau}$ -chart | $\tilde{\kappa}$ -chart | $\hat{\rho}$ -chart |
|--------|------------|------------|------------|---------------------|-----------------------|-----------------------|-------------------------|---------------------|
| 10, 10 | 0.1 | 0.1 | 0.1 | 160.16 | 122.85 | 92.96 | 332.93 | 437.13 |
| 15, 15 | | | | 94.15 | 64.34 | 46.3 | 315.38 | 197.22 |
| 25, 25 | | | | 41.06 | 26.8 | 19.17 | 267.66 | 69.41 |
| 40, 25 | | | | 27.65 | 18.19 | 13.33 | 233.61 | 43.22 |
| 10, 10 | 0.2 | 0.2 | 0.2 | 48.43 | 40.53 | 26.6 | 224.04 | 37.57 |
| 15, 15 | | | | 24.59 | 20.09 | 13.73 | 158.31 | 15.03 |
| 25, 25 | | | | 11.21 | 9.35 | 6.8 | 82.51 | 6.64 |
| 40, 25 | | | | 8.16 | 6.89 | 5.14 | 56.99 | 4.92 |
| 10, 10 | 0.2 | 0.2 | 0.5 | 52.44 | 281.82 | 295.92 | 51.45 | 2.68 |
| 15, 15 | | | | 26.51 | 202.89 | 207.22 | 26.11 | 1.79 |
| 25, 25 | | | | 12.09 | 108.6 | 109.4 | 11.83 | 1.02 |
| 40, 25 | | | | 8.73 | 75.15 | 75.99 | 8.58 | 1.0 |
| 10, 10 | 0.4 | 0.3 | 0.1 | 9.86 | 8.85 | 6.3 | 57.27 | 8.71 |
| 15, 15 | | | | 5.88 | 5.32 | 3.96 | 30.35 | 4.49 |
| 25, 25 | | | | 3.35 | 3.09 | 2.38 | 13.84 | 2.47 |
| 40, 25 | | | | 2.65 | 2.45 | 2.02 | 9.95 | 2.02 |

NOTE: The table's largest standard error for the ARL is 1.36.

Table A.5: OOC-ARLs of EWMA SOP-charts and competing $\hat{\rho}$ -chart for unilateral SINAR(1, 1) model like in Table A.1, smoothing parameter $\lambda = 0.1$, but with ZIP(0.9, 5) innovations; simulated with 10^5 replications.

| m, n | α_1 | α_2 | α_3 | $\hat{\tau}$ -chart | $\hat{\kappa}$ -chart | $\tilde{\tau}$ -chart | $\tilde{\kappa}$ -chart | $\hat{\rho}$ -chart |
|--------|------------|------------|------------|---------------------|-----------------------|-----------------------|-------------------------|---------------------|
| 10, 10 | 0.1 | 0.1 | 0.1 | 6.21 | 5.85 | 4.26 | 29.92 | 9.63 |
| 15, 15 | | | | 3.93 | 3.71 | 2.82 | 15.89 | 5.08 |
| 25, 25 | | | | 2.36 | 2.25 | 1.96 | 7.84 | 2.8 |
| 40, 25 | | | | 2.01 | 1.97 | 1.52 | 5.9 | 2.22 |
| 10, 10 | 0.2 | 0.2 | 0.2 | 3.7 | 4.77 | 3.17 | 9.07 | 3.15 |
| 15, 15 | | | | 2.48 | 3.11 | 2.13 | 5.48 | 2.05 |
| 25, 25 | | | | 1.72 | 2.02 | 1.38 | 3.16 | 1.13 |
| 40, 25 | | | | 1.2 | 1.78 | 1.01 | 2.52 | 1.0 |
| 10, 10 | 0.2 | 0.2 | 0.5 | 5.11 | 298.41 | 15.2 | 5.72 | 1.57 |
| 15, 15 | | | | 3.32 | 214.87 | 8.59 | 3.66 | 1.0 |
| 25, 25 | | | | 2.09 | 113.44 | 4.64 | 2.25 | 1.0 |
| 40, 25 | | | | 1.78 | 78.24 | 3.6 | 1.91 | 1.0 |
| 10, 10 | 0.4 | 0.3 | 0.1 | 2.37 | 3.29 | 2.11 | 4.71 | 2.46 |
| 15, 15 | | | | 1.8 | 2.2 | 1.75 | 3.08 | 1.64 |
| 25, 25 | | | | 1.0 | 1.51 | 1.0 | 2.0 | 1.0 |
| 40, 25 | | | | 1.0 | 1.02 | 1.0 | 1.68 | 1.0 |

NOTE: The table's largest standard error for the ARL is 0.92.

Table A.6: OOC-ARLs of EWMA SOP-charts and competing $\hat{\rho}$ -chart for unilateral SQMA(1,1)-model for $\beta_1 = \beta_2 = \beta_3 = 0.8$, different m, n combinations, smoothing parameter $\lambda = 0.1$, and target $ARL_0 \approx 370$; simulated with 10^5 replications.

| m, n | Model | $\hat{\tau}$ -chart | $\hat{\kappa}$ -chart | $\tilde{\tau}$ -chart | $\tilde{\kappa}$ -chart | $\hat{\rho}$ -chart |
|--------|---|---------------------|-----------------------|-----------------------|-------------------------|---------------------|
| 10, 10 | "1 ² 2 ² 3 ² " | 13.64 | 8.87 | 6.9 | 165.91 | 79.13 |
| 15, 15 | | 7.78 | 5.33 | 4.29 | 108.8 | 85.5 |
| 25, 25 | | 4.25 | 3.09 | 2.56 | 52.0 | 90.03 |
| 40, 25 | | 3.32 | 2.45 | 2.09 | 35.57 | 91.58 |
| 10, 10 | "1 ² 2 ¹ 3 ² " | 7.86 | 4.67 | 3.92 | 168.38 | 87.33 |
| 15, 15 | | 4.83 | 3.06 | 2.61 | 130.93 | 84.24 |
| 25, 25 | | 2.83 | 2.0 | 1.89 | 78.02 | 80.73 |
| 40, 25 | | 2.27 | 1.73 | 1.3 | 57.22 | 79.96 |
| 10, 10 | "1 ¹ 2 ¹ 3 ² " | 7.37 | 7.45 | 5.16 | 32.62 | 79.01 |
| 15, 15 | | 4.56 | 4.58 | 3.34 | 17.25 | 84.12 |
| 25, 25 | | 2.69 | 2.7 | 2.08 | 8.42 | 87.19 |
| 40, 25 | | 2.18 | 2.17 | 1.89 | 6.27 | 87.81 |
| 10, 10 | "1 ² 2 ¹ 3 ¹ " | 12.58 | 10.79 | 7.68 | 82.82 | 4.13 |
| 15, 15 | | 7.3 | 6.35 | 4.72 | 44.64 | 2.59 |
| 25, 25 | | 4.02 | 3.58 | 2.78 | 19.6 | 1.76 |
| 40, 25 | | 3.15 | 2.83 | 2.22 | 13.77 | 1.2 |

NOTE: The table's largest standard error for the ARL is 0.51. Label "1^a 2^b 3^c" indicates which MA-terms are squared.

Table A.7: OOC-ARLs of EWMA SOP-charts and competing $\hat{\rho}$ -chart for unilateral SQINMA(1, 1)-model with i. i. d. Poi(5)-innovations ϵ_{t_1, t_2} and $\beta_1 = \beta_2 = \beta_3 = 0.8$, different m, n combinations, smoothing parameter $\lambda = 0.1$, and target $ARL_0 \approx 370$; simulated with 10^5 replications.

| m, n | Model | $\hat{\tau}$ -chart | $\hat{\kappa}$ -chart | $\tilde{\tau}$ -chart | $\tilde{\kappa}$ -chart | $\hat{\rho}$ -chart |
|--------|---|---------------------|-----------------------|-----------------------|-------------------------|---------------------|
| 10, 10 | “1 ² 2 ² 3 ² ” | 4.92 | 6.3 | 4.09 | 13.45 | 138.17 |
| 15, 15 | | 3.2 | 3.96 | 2.72 | 7.78 | 45.14 |
| 25, 25 | | 2.04 | 2.38 | 1.92 | 4.26 | 14.55 |
| 40, 25 | | 1.78 | 2.02 | 1.42 | 3.33 | 9.78 |
| 10, 10 | “1 ² 2 ¹ 3 ² ” | 5.06 | 4.58 | 3.45 | 24.12 | 53.25 |
| 15, 15 | | 3.28 | 3.0 | 2.3 | 13.34 | 18.72 |
| 25, 25 | | 2.07 | 1.99 | 1.65 | 6.8 | 7.77 |
| 40, 25 | | 1.81 | 1.7 | 1.05 | 5.14 | 5.65 |
| 10, 10 | “1 ¹ 2 ¹ 3 ² ” | 45.04 | 78.89 | 39.23 | 128.63 | 12.36 |
| 15, 15 | | 22.96 | 39.15 | 19.56 | 72.88 | 6.34 |
| 25, 25 | | 10.63 | 16.69 | 9.18 | 31.51 | 3.38 |
| 40, 25 | | 7.75 | 11.71 | 6.77 | 21.53 | 2.65 |
| 10, 10 | “1 ² 2 ¹ 3 ¹ ” | 23.85 | 47.63 | 22.0 | 67.97 | 484.57 |
| 15, 15 | | 12.75 | 23.37 | 11.67 | 35.35 | 351.6 |
| 25, 25 | | 6.45 | 10.61 | 5.96 | 15.66 | 144.19 |
| 40, 25 | | 4.88 | 7.73 | 4.54 | 11.12 | 89.31 |

NOTE: The table’s largest standard error for the ARL is 1.5. Label “1^a 2^b 3^c” indicates which MA-terms are squared.

Table A.8: OOC-ARLs of EWMA SOP-charts and competing $\hat{\rho}$ -chart for bilateral SAR(1)-model for different m, n, a_1, a_2, a_3, a_4 combinations, smoothing parameter $\lambda = 0.1$, and target $ARL_0 \approx 370$; simulated with 10^5 replications.

| m, n | a_1 | a_2 | a_3 | a_4 | $\hat{\tau}$ -chart | $\hat{\kappa}$ -chart | $\tilde{\tau}$ -chart | $\tilde{\kappa}$ -chart | $\hat{\rho}$ -chart |
|--------|-------|-------|-------|-------|---------------------|-----------------------|-----------------------|-------------------------|---------------------|
| 10, 10 | 0.1 | 0.1 | 0.1 | 0.1 | 8.77 | 10.92 | 6.81 | 30.42 | 36.47 |
| 15, 15 | | | | | 5.31 | 6.37 | 4.25 | 16.23 | 12.98 |
| 25, 25 | | | | | 3.07 | 3.58 | 2.53 | 7.93 | 5.7 |
| 40, 25 | | | | | 2.45 | 2.83 | 2.08 | 5.95 | 4.26 |
| 10, 10 | 0.05 | 0.05 | 0.15 | 0.15 | 8.86 | 10.98 | 6.85 | 30.74 | 30.84 |
| 15, 15 | | | | | 5.36 | 6.42 | 4.27 | 16.34 | 11.53 |
| 25, 25 | | | | | 3.09 | 3.6 | 2.54 | 8.01 | 5.23 |
| 40, 25 | | | | | 2.46 | 2.85 | 2.09 | 6.0 | 3.93 |
| 10, 10 | 0.05 | 0.15 | 0.05 | 0.15 | 8.85 | 11.01 | 6.87 | 30.75 | 46.61 |
| 15, 15 | | | | | 5.35 | 6.41 | 4.27 | 16.36 | 15.31 |
| 25, 25 | | | | | 3.09 | 3.61 | 2.55 | 8.03 | 6.43 |
| 40, 25 | | | | | 2.46 | 2.85 | 2.08 | 6.0 | 4.73 |

NOTE: The table's largest standard error for the ARL is 0.12.

Table A.9: OOC-ARLs of EWMA SOP-charts and competing $\hat{\rho}$ -chart for bilateral SAR(1)-model like in Table A.8, smoothing parameter $\lambda = 0.1$, but where 10% of observations are contaminated by AOs; simulated with 10^5 replications.

| m, n | a_1 | a_2 | a_3 | a_4 | $\hat{\tau}$ -chart | $\hat{\kappa}$ -chart | $\tilde{\tau}$ -chart | $\tilde{\kappa}$ -chart | $\hat{\rho}$ -chart |
|--------|-------|-------|-------|-------|---------------------|-----------------------|-----------------------|-------------------------|---------------------|
| 10, 10 | 0.1 | 0.1 | 0.1 | 0.1 | 19.28 | 14.52 | 10.37 | 146.32 | 371.24 |
| 15, 15 | | | | | 10.55 | 8.13 | 6.12 | 90.48 | 115.7 |
| 25, 25 | | | | | 5.5 | 4.41 | 3.47 | 41.88 | 33.06 |
| 40, 25 | | | | | 4.22 | 3.43 | 2.74 | 28.51 | 20.72 |
| 10, 10 | 0.05 | 0.05 | 0.15 | 0.15 | 19.45 | 14.63 | 10.46 | 147.33 | 336.06 |
| 15, 15 | | | | | 10.65 | 8.2 | 6.17 | 91.41 | 101.0 |
| 25, 25 | | | | | 5.55 | 4.43 | 3.49 | 42.33 | 29.18 |
| 40, 25 | | | | | 4.25 | 3.45 | 2.76 | 28.93 | 18.62 |
| 10, 10 | 0.05 | 0.15 | 0.05 | 0.15 | 19.5 | 14.58 | 10.47 | 147.77 | 426.56 |
| 15, 15 | | | | | 10.68 | 8.19 | 6.19 | 91.35 | 141.25 |
| 25, 25 | | | | | 5.55 | 4.43 | 3.49 | 42.13 | 40.18 |
| 40, 25 | | | | | 4.25 | 3.46 | 2.76 | 28.94 | 24.73 |

NOTE: The table's largest standard error for the ARL is 1.32.

Table A.10: OOC-ARLs of EWMA SOP-charts and competing $\hat{\rho}$ -chart for bilateral SQMA(1)-model for $b_1 = \dots = b_4 = 0.8$, for different m, n combinations, smoothing parameter $\lambda = 0.1$, and target $ARL_0 \approx 370$; simulated with 10^5 replications.

| m, n | Model | $\hat{\tau}$ -chart | $\hat{\kappa}$ -chart | $\tilde{\tau}$ -chart | $\tilde{\kappa}$ -chart | $\hat{\rho}$ -chart |
|--------|--|---------------------|-----------------------|-----------------------|-------------------------|---------------------|
| 10, 10 | “1 ² 2 ² 3 ² 4 ² ” | 43.3 | 28.49 | 34.5 | 32.68 | 37.11 |
| 15, 15 | | 30.67 | 17.63 | 26.68 | 18.27 | 33.68 |
| 25, 25 | | 17.66 | 9.45 | 17.16 | 9.1 | 31.13 |
| 40, 25 | | 13.31 | 7.16 | 13.42 | 6.78 | 30.34 |
| 10, 10 | “1 ² 2 ¹ 3 ² 4 ¹ ” | 12.83 | 5.68 | 5.05 | 405.43 | 48.05 |
| 15, 15 | | 7.4 | 3.65 | 3.28 | 296.66 | 41.95 |
| 25, 25 | | 4.07 | 2.24 | 2.07 | 156.89 | 38.11 |
| 40, 25 | | 3.19 | 1.91 | 1.77 | 108.16 | 36.94 |
| 10, 10 | “1 ² 2 ² 3 ¹ 4 ¹ ” | 11.82 | 6.05 | 5.23 | 421.68 | 6.14 |
| 15, 15 | | 6.98 | 3.86 | 3.39 | 414.0 | 3.6 |
| 25, 25 | | 3.89 | 2.35 | 2.13 | 409.19 | 2.15 |
| 40, 25 | | 3.07 | 1.97 | 1.79 | 403.95 | 1.82 |

NOTE: The table’s largest standard error for the ARL is 1.31. Label “1^a 2^b 3^c 4^d” indicates which MA-terms are squared.